
A SENSOR INVARIANT ATMOSPHERIC CORRECTION: SENTINEL-2/MSI AND LANDSAT 8/OLI

Feng Yin^{1*}, Philip E Lewis^{1,2}, Jose L Gómez-Dans^{1,2} Qingling Wu¹

1 Department of Geography, University College London, Gower Street, London WC1E 6BT, United Kingdom

2 National Centre for Earth Observation (NCEO), NERC, United Kingdom

* Corresponding author: feng.yin.15@ucl.ac.uk

Abstract

Mitigating the impact of atmospheric effects on optical data is a critical for monitoring land processes. Consistent approaches to different sensors, which also quantify uncertainty, are required to combine surface reflectance observations from heterogeneous sensors. This paper provides a sensor agnostic approach to atmospheric correction, called SIAC. It exploits operational global datasets on (i) coarse resolution spectral surface bi-directional reflectance distribution function (BRDF) and (ii) coarse resolution atmospheric composition. The method infers aerosol optical thickness (AOT) and total columnar water vapour (TCWV) from top of atmosphere (TOA) reflectance observations, using a Bayesian framework that exploits the MODIS MCD43 BRDF descriptor product and the Copernicus Atmosphere Monitoring Service (CAMS) operational forecasts of AOT and TCWV to provide an *a priori* estimate. Spatial smoothness constraints are assumed for AOT and TCWV, and efficient statistical approximations (so-called emulators) to atmospheric radiative transfer (RT) codes are used to efficiently invert the parameters. BRDF descriptors are used to provide an estimation of surface directional reflectance (SDR) at a coarse resolution, and linear spectral mappings to convert to the target sensor spectral configuration. The method is demonstrated on Sentinel 2 and Landsat 8 data. AOT retrieval for both S2 and L8 shows a very high correlation to AERONET estimates ($r^2 > 0.9$, $RMSE < 0.025$ for both sensors), although with a small underestimate of AOT. TCWV is accurately retrieved from both sensors ($r^2 > 0.95$, $RMSE < 0.02$). Comparisons with *in situ* surface

1
2
3
4
5
6
7
8
9
10
11
12
13
14
15
16
17
18
19
20
21
22
23
24
25
26
27
28

reflectance measurements from the RadCalNet network show that the proposed method provides accurate estimates of surface reflectance across the entire spectrum, with *RMSE* mismatches with the reference data between 0.005 and 0.02 in units of reflectance, both for Sentinel 2 and Landsat 8. For near-simultaneous Sentinel-2 and Landsat-8 acquisitions, there is a very tight relationship ($r^2 > 0.95$ for all common bands) between surface reflectance acquired from both sensors, with no negligible biases.

Keywords — Atmospheric correction; Sentinel 2; Landsat 8; Analysis-ready data ; Inverse problems

1 Introduction

Satellite observations of the land surface have long been used to provide objective and reliable information about Earth system processes and to enhance predictions of the evolution of important variables related to climate, land surface and hydrological processes (CEOS, 2013; Pfeifer et al., 2012). Land surface reflectance is the most fundamental magnitude used to infer land surface processes, but satellite measurements are contaminated by the inevitable influence of atmospheric processes, such as the scattering and absorption of radiation by clouds, aerosols and gases. It is important to be able to compensate or correct for these atmospheric effects to produce a record of surface reflectance (Fraser and Kaufman, 1985; Vermote et al., 1997). Further interpretation of land surface reflectance requires not only an accurate estimate of this magnitude, but also consistency between different data products, and uncertainty information on the quality of the corrected surface reflectance (Doxani et al., 2018; Wulder et al., 2015).

Over the last few decades, a number of techniques have been introduced to perform atmospheric correction. These range from simple empirical methods to methods that aim to use physical models to understand the physical processes that affect photons in the atmosphere. An early method for atmospheric correction is the dark object subtraction (DOS) method (Chavez et al., 1996): under the assumption that for very dark areas, the measured radiance is equal to the path radiance. This path radiance can then be subtracted for all other pixels in the image. The main assumptions are that the path radiance is constant across the image and that there are no multiple scattering effects (Ju et al., 2012). Improving on this, methods based on the presence dark dense vegetation (DDV) patches (due to strong absorption in the visible region of the spectrum, regions with dark

dense vegetation appear very dark) (Kaufman et al., 1997; Vermote et al., 1997; Remer et al., 2005; Levy et al., 2007b,a). For these areas, an empirical relationship between the surface reflectance in the SWIR region (e.g. around 2100 μm and reflectance in the blue and red bands is used to provide an estimate of surface reflectance in the visible part of the spectrum. These estimates are then used to invert the 6S (Vermote et al., 1997) radiative transfer (RT) model and provide an estimate of the main atmospheric effects affecting most multi-spectral sensors: aerosol optical thickness (AOT), total columnar water vapour (TCWV) and total columnar ozone (TCO₃). Once these atmospheric constituents are known, their effect can be removed from the top of atmosphere (TOA) observations. It is worth noting that the LEDAPS atmospheric correction method (Ju et al., 2012; Masek et al., 2012) shares a lot with the MODIS atmospheric correction method. The DDV method has been complemented by the Deep Blue approach of Hsu et al. (2004, 2013), which is based on a seasonally-resolved global reflectance database produced by the minimum reflectivity technique over bright surfaces.

Recently, a number of methods have started exploiting the fact that the evolution of the land surface properties is slow in the scale of days. Hence, for two temporally close (e.g. a few days' difference) acquisitions (and in the absence of other complicating factors, such as BRDF effects), the changes in TOA reflectance are due to differences in atmospheric composition. Liang et al. (2006) developed an algorithm based on this idea. Comparisons of retrieved AOT with *in situ* AERONET measurements showed good agreement. A more sophisticated method was developed in (Lyapustin et al., 2011a,b, 2012). Lyapustin's method relies on the use of semi-empirical linear kernel models to model angular effects over short temporal periods. Hagolle et al. (2015) used empirical linear relationship between spectral bands to get the surface reflectance at visible bands, and a temporal constrain is also used under the concept of relative invariant surface reflectance mentioned above. As the method is used for high spatial resolution images (e.g. Landsat or Sentinel-2), the presence of clouds can result in consecutive observations been temporally far apart, which will hamper the proposed method. The method of Guanter et al. (2007) uses a linear combination of spectra to predict the surface reflectance, and then uses a look-up table to perform the inference of atmospheric composition parameters. Finally, the CISAR method of Luffarelli et al. (2017) uses a Bayesian optimal estimation (OE) framework which exploits the slow changes in the land surface, as well as other sources of prior information, to correct PROBA-V observations.

The two recently launched Sentinel 2 (S2) (S2A and S2B) satellites

by European Space Agency (ESA) together with the Landsat 8 from the
National Aeronautics and Space Administration (NASA) and U.S.
Geological Survey (USGS) provide moderate-to-high spatial resolution
(10 m–30 m) multi-spectral satellite images under free and open data
policy. Several atmospheric correction schemes have been developed
for different applications (for a complete review, please refer to [Doxani
et al. \(2018\)](#)), but most have been generally developed with a single
sensor in mind, hence limiting the consistency between surface
reflectance derived from S2 and L8. Also, only limited attention has
been provided to uncertainty quantification.

The methods proposed for atmospheric correction previously aim to
simplify the surface-atmospheric coupling by using some known
properties (e.g. correlations between reflectance on different bands
over known targets, previous observations, linear models, ...) to
prescribe or approximate the land surface reflectance in the visible
bands (where aerosol effects are dominant). With this expectation of
surface reflectance, a RT model is then used to forward model the
surface reflectance to TOA reflectance as a function of aerosol
abundance. This last step is usually accomplished by means of a
look-up table. Other important absorption gases (e.g. TCWV, TCO₃)
are sometimes prescribed from re-analysis data (e.g. [Masek et al.
\(2012\)](#)). Additionally, most methods exploit the observation that most
atmospheric constituents have large (~ 10s of km) correlation lengths,
usually by assuming atmospheric composition constant over several
pixels.

This contribution builds on the previous efforts to develop a method
that is designed to provide consistent estimates of land surface
reflectance from different high resolution optical sensors. The
proposed method exploits the opportunities offered by new data sets
describing the spectral land surface anisotropy over global scales at
moderate resolution (for example, the MODIS MCD43 product from
[Schaaf et al. \(2002\)](#); [C. Schaaf \(2015\)](#)), as well as predictions of aerosol
abundance and type, as well as other atmospheric gas concentrations
operationally provided by services such as the Copernicus Atmosphere
Monitoring Service (CAMS,) ([Eskes et al., 2018](#)). These two sources of
information are in effect used as *a priori* distributions in a Bayesian
inverse problem set-up ([Lewis et al., 2012](#); [Gómez-Dans et al., 2016](#)).
The aim of this problem is to infer the *a posteriori* distribution of
atmospheric composition inverting an atmospheric RT model. The
Bayesian approach inherently deals with input data uncertainty
([Gorroño et al., 2018](#)) and prior parameter uncertainty, providing an
estimate of surface reflectance uncertainty. For the sake of
computational efficiency, emulators, fast surrogates to complex

numerical models (Gómez-Dans et al., 2016) are used instead of the full RT model.

In this paper, we present the theoretical underpinnings of the method, implementation and provide a demonstration on S2 and LC8 data. The method is validated on the basis of comparisons of AOT with *in situ* AERONET measurements, comparisons of retrieved surface reflectance with *in situ* RadCalNet measurements, as well as comparisons of surface reflectance between S2 and LC8.

2 Method

2.1 General description of the proposed method

As outlined in the Introduction, we propose using a spectral BRDF descriptor dataset that describes the land surface anisotropy as well as a prior estimate of atmospheric composition to solve an inverse problem. The method has the following steps:

1. Use the BRDF descriptors data set to provide an expectation of the surface reflectance at the target sensor acquisition geometry at coarse resolution and in the BRDF descriptor bands
2. Using a set of linear transformations, convert the predicted surface reflectance from the previous step to the target sensor spectral bands. At this stage, we have an expectation of surface reflectance for the target geometry and spectral bands at coarse resolution.
3. Under the assumption of very strong correlation between the bottom and top of the atmosphere reflectances infer an empirical point spread function (PSF) model by maximising the correlation between TOA reflectances convolved with a Gaussian PSF and the BOA coarse resolution expectation.
4. At this stage, we can map the surface reflectances to the top of the atmosphere using a suitable RT model and estimates of atmospheric composition. These can be compared with the measured target sensor TOA reflectances convolved with the empirical PSF.
5. Exploiting the CAMS data as a prior distribution, we build an inverse problem to solve for AOT, TCWV and TCO₃. Further, spatial regularisation is used to under the assumption of smooth variation of atmospheric composition parameters.

The previous steps result in a complete inference on the *a posteriori* joint pdf of the atmospheric parameters, which can then be used to correct the original TOA reflectance data using the Lambertian surface-atmosphere coupling assumption.

2.2 Spectral mapping

Spectral correlation over most natural surfaces suggests that transformations between different spectral domains are possible. In Liang (2001), a set of linear transformations are used to transform from narrowband (sensor) bands to broadbands. We extend this idea to map MODIS, Sentinel-2 and Landsat bands by the using of linear model. A database of spectra from the ESA ADAM project (Muller et al., 2013) are used as an input to infer the transformations. For each sensor, the spectra are convolved with the relative spectral response (RSR) functions. This produces sets of the same spectra as observed with different sensor spectral properties. A linear mapping between pairs of sensors is then obtained from these data. This conversion matrix can be used to convert measurements acquired with one sensor spectral sampling to another sensor bands. As the mapping is linear, uncertainty propagation is well understood.

In more detail, if the full spectral data are given by $\rho(\lambda_F)$, one can model an arbitrary sensor band λ_M just by multiplying the full spectrum by the relevant RSR function:

$$\rho(\lambda_M) = \rho(\lambda_F) \times RSR(\lambda_M) \quad (1)$$

Stacking all the database predictions from sensor $s1$ in a matrix \mathbf{X}_{s1} , and doing the same with database predictions from another sensor $s2$, a linear model can be written as

$$\mathbf{X}_{s1} \cdot \hat{\beta} = \mathbf{X}_{s2} \quad (2)$$

The solution of this is well known

$$\hat{\beta} = (\mathbf{X}_{s1}^T \cdot \mathbf{X}_{s1})^{-1} \cdot \mathbf{X}_{s2} \quad (3)$$

The prediction of a new sample in $s2$ bands when the sample spectrum is known in the $s1$ bands is given by

$$\mathbf{X}_{s2_new} = \mathbf{X}_{s1_new} \cdot \hat{\beta} \quad (4)$$

In order to assess the uncertainty of the mapping, we can calculate the covariance matrix of the mapping as

$$\mathbf{V}(\mathbf{X}_{s2}|\mathbf{X}_{s1}) = \sum \mathbf{V}(\mathbf{X}_{s2} - \mathbf{X}_{s1} \cdot \hat{\beta})^2 \quad (5)$$

Finally, we can calculate the predictive uncertainty as

222

$$\mathbf{V}(\mathbf{X}_{s2_new}|\mathbf{X}_{s1_new}) = \mathbf{V}(\mathbf{X}_{s2}|\mathbf{X}_{s1}) \cdot (1 + \mathbf{X}_{s1_new} \cdot (\mathbf{X}_{s1}^T \cdot \mathbf{X}_{s1})^{-1} \cdot \mathbf{X}_{s1_new}^T) \quad (6)$$

For simplicity, we assume the predictive uncertainty covariance matrix to be purely diagonal.

223

224

$$\sigma^2 = \mathbf{diag}(\mathbf{V}(\mathbf{X}_{s2_new}|\mathbf{X}_{s1_new})) \quad (7)$$

2.3 Point Spread Function (PSF) modelling

225

Due to the big differences in the spatial resolution between the MODIS (500 m) and S2/LC8 (10.20 m and/or 30 m) the measured reflectance values from them can not be directly compared. We model the MODIS data effective PSF, and use this to convolve the high resolution data in order to make it comparable with the MODIS products. Ideally, the MODIS cross track direction PSF is triangular and rectangular in along track direction, (Tan et al., 2006; Schowengerdt, 2006), as a result of optical PSF_{opt} , detector PSF_{det} , image motion PSF_{im} , electronics PSF_{el} .

226

227

228

229

230

231

232

233

$$PSF_{net}(x, y) = PSF_{opt} * PSF_{det} * PSF_{im} * PSF_{el} \quad (8)$$

As we are using the MODIS MCD43 BRDF products to simulate the surface reflectance, which is a composition of 16 days measurements from different angles with different scanning geometry, the equivalent PSF ($ePSF$) is estimated by assuming it is a two-dimensional Gaussian (Kaiser and Schneider, 2008; Duveiller et al., 2011; Mira et al., 2015) in along track and cross track directions, shown in Figure 1.

234

235

236

237

238

239

$$ePSF(x, y) = \exp\left(-\frac{(x + Shift_x)^2}{2\sigma_x^2}\right) \cdot \exp\left(-\frac{(y + Shift_y)^2}{2\sigma_y^2}\right) \quad (9)$$

Where σ_x and σ_y are the standard deviation of Gaussian function expressed over satellite image pixels unit, $Shift_x$ and $Shift_y$ represent the shifts in along and cross directions. According to (Duveiller et al., 2011; Capderou, 2005) there is also an angular deviation between the satellite orbit and the true north, which is given by:

240

241

242

243

244

$$\tan \theta = \frac{\cos i - (1/\kappa) \cos^2 \varphi}{\sqrt{\cos^2 \varphi - \cos^2 i}} \quad (10)$$

Where θ is the angular deviation, i is the inclination angle, φ is the latitude and κ is the daily recurrence frequency. Then the rotation matrix (R_θ) is:

245

246

247

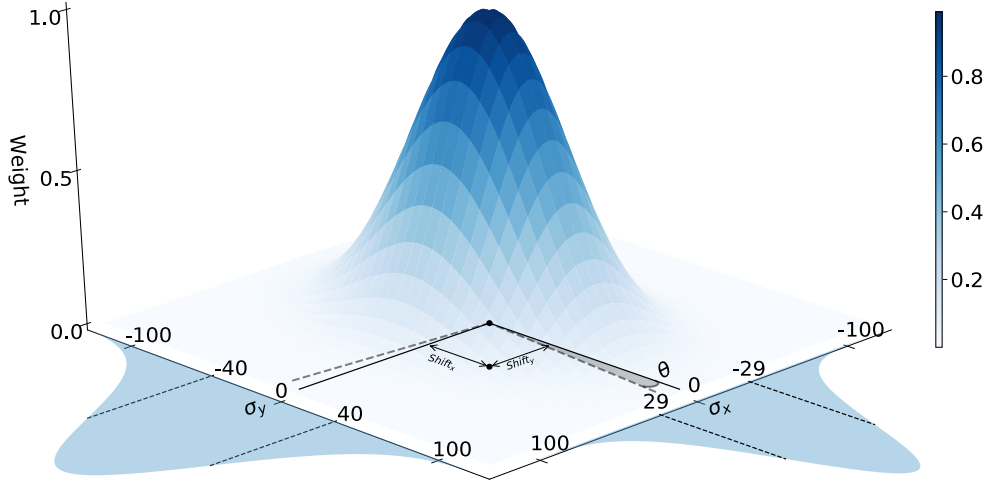


Figure 1. A typical MODIS *ePSF* on the spatial resolution of S2, *i.e.* unit of 1 represent 10 m on the X–Y plane, and it follows the same notations as in Equation 9–11. The shaded area on the two sides represent the Gaussian functions used for x and y directions, with 1 σ shown with vertical dash lines.

$$R_{\theta} = \begin{bmatrix} \cos \theta & -\sin \theta \\ \sin \theta & \cos \theta \end{bmatrix} \quad (11)$$

At this stage, it is possible to arrive at an expression that will allow the comparison of the high resolution TOA reflectance with the coarse resolution predictions of surface reflectance obtained from the MCD43 product propagated through the atmosphere. This step is a fundamental stage in defining how the proposed method solves for atmospheric composition, and the equality requires that the high resolution data (S2/L8) are convolved with the *ePSF*. Given the disparity of spatial resolutions, the S2/L8 PSF effect is neglected.

$$\rho_{toa_simu}(x_m, y_m, \lambda, \Omega, \Omega') = \rho_{toa}(x, y, \lambda, \Omega, \Omega') * (R_{\theta} \cdot ePSF(x, y)) \quad (12)$$

where $\rho_{toa_simu}(x_m, y_m, \lambda, \Omega, \Omega')$ is the simulated specific band (λ) TOA reflectance value at MODIS resolution (x_m and y_m) at S2/L8 scanning geometry (Ω and Ω') and $\rho_{toa}(x, y, \lambda_M, \Omega, \Omega')$ is the S2/L8 TOA reflectance. Making use of Eq. 4, we can convert the S2/L8 spectral bands to MODIS bands:

$$\rho_{toa_simu}(x_m, y_m, \lambda_M, \Omega, \Omega') = \rho_{toa_pred}(x_m, y_m, \lambda, \Omega, \Omega') \cdot \hat{\beta}. \quad (13)$$

The definition of ρ_{toa_pred} , the predicted TOA reflectance propagated through the atmosphere with an atmospheric radiative transfer model f is given by

$$\rho_{toa_pred}(x_m, y_m, \lambda_M, \Omega, \Omega') = H(\rho_{pred}(x_m, y_m, \lambda_M, \Omega, \Omega')) \quad (14)$$

In this study, $H(\cdot)$ is the 6S model from [Vermote et al. \(1997\)](#)

2.4 Atmospheric effects modelling and estimation of $ePSF$

Assuming a Lambertian homogeneous surface with surface reflectance at sea level altitude ([Gómez-Dans et al., 2016](#); [Guanter et al., 2009](#); [Vermote et al., 1997](#)), the coupling of surface and atmosphere can be written as:

$$L_{toa} = L_p + \frac{\rho E_d T_t}{\pi(1 - S\rho)} \quad (15)$$

Where L_{toa} , L_p , ρ , E_d , T_t and S are the TOA radiance, atmospheric path radiance, intrinsic surface reflectance, total radiance reaching earth surface captured by the image, total transmittance including upward and downward parts and atmospheric single scattering albedo coming from the multiple scattering between the earth surface and atmosphere, individually. Eq. 15 can be expressed in terms of reflectance as

$$\rho_{toa}(\Omega, \Omega') = \rho_p + \frac{\rho \cdot T_t(\Omega, \Omega')}{1 - S\rho} \quad (16)$$

where $\rho_{toa}(\Omega, \Omega')$ is the apparent TOA reflectance, ρ_p is the atmospheric path reflectance. Combining this with Eq. 14, we have that

$$\rho_{toa_simu}(x_m, y_m, \lambda_M, \Omega, \Omega') = \rho_p + \frac{\rho_{pred}(x_m, y_m, \lambda_M, \Omega, \Omega') \cdot T_t(\Omega, \Omega')}{1 - S \cdot \rho_{pred}(x_m, y_m, \lambda_M, \Omega, \Omega')} \quad (17)$$

It is worth examining the form of Eq. 17 and see the shape of the relationship between ρ_{pred} and the associated ρ_{toa} . The path radiance is a bias term, whereas the second term in the right hand side of Eq. 17 suggests a non-linear coupling. However, for low to moderate values of AOT and ρ_{pred} , this relationship can be very well approximated by a linear. Over natural surfaces thus, we expect a strong correlation between ρ_{pred} and ρ_{toa} . Over the near- and short-wave infrared (NIR

and SWIR) regions, the small effect of aerosols will make the relationship strongly linear and with a small bias as ρ_p would be very small.

This expected correlation between top of atmosphere measurements and bottom of atmosphere predictions allows us to infer the shape of the effective point spread function by maximising the correlation between $\rho_{toa,imu}(x_m, y_m, \lambda_{SWIR}, \Omega, \Omega')$ (Eq. 12 and the predicted reflectance $\rho_{pred}(x_m, y_m, \lambda_{SWIR}, \Omega, \Omega')$ from MCD43 in the SWIR region. Assuming the retrieved *ePSF* parameters are constant for all bands, the retrieved *ePSF* shape is then applied to other bands by simple convolution. This step provides a linkage between a coarse spatial resolution of the land surface and the top of atmosphere target sensor directional reflectance observations.

2.5 Inferring the atmospheric composition

The previous sections detail how the TOA reflectance from the level 1C S2 or L8 products can be related with an expectation of surface reflectance at coarse spatial resolution coming from the MCD43 product. The last step is solving for atmospheric composition parameters. This approach mainly involves modifying the atmospheric composition parameters assumed for $H(\cdot)$ in Eq. 14 until the propagated surface reflectance predictions match the TOA reflectance convolved with the effective *PSF*, taking into account the uncertainty of both the TOA measurements and predictions. Under the assumption of these uncertainties being Gaussian, the log-likelihood function can be written as a simple cost function

$$J_{obs}(x) = \frac{1}{2}(R - H(x|x_c))^T C_{obs}^{-1}(R - H(x|x_c)), \quad (18)$$

where x is a vector containing the atmospheric composition parameters (AOT, TCWV, TCO3) over a spatial grid, H is the atmospheric radiative transfer model, x_c are ancillary variables required to run the model (e.g. target elevation, view and illumination geometry, and predicted surface reflectance from MCD43). C_{obs} is the covariance matrix that describes the uncertainties on both observations and predictions. Minimising J_{obs} as a function of x results in an ill-posed problem, which can be ameliorated by a Bayesian approach, where additional constraints on the parameters are included as prior information (Lewis et al., 2012; Gómez-Dans et al., 2016; Kaminski et al., 2017).

We focus on two prior constraints: (i) a prior expectation of the atmospheric parameter distribution from the Copernicus Atmospheric Monitoring Service (CAM5), and (ii) an expectation of spatial

correlation of atmospheric composition parameters, which results in spatially smooth fields of e.g. AOT or TCWV. 326
327

The CAMS parameter constraint is encoded as a Gaussian prior distribution, characterised by a mean vector and a covariance matrix (assumed diagonal here). The resulting cost function is given by 328
329
330

$$J_{prior}(x) = \frac{1}{2}(x - x_{prior})^T C_{prior}^{-1}(x - x_{prior}). \quad (19)$$

The expectation of spatial smoothness is analogous to the expectation of temporal smoothness shown in Lewis et al. (2012); Gómez-Dans et al. (2016). Assuming a differential operator D , the relevant part of the cost function is given by 331
332
333
334

$$J_{model}(x) = \frac{\gamma^2}{2} x^T (D^T D)x, \quad (20)$$

which basically encodes that spatial differences among neighbouring grid cells are normally distributed with zero mean and a variance given by $1/\gamma^2$. 335
336
337

Assuming that the two prior constraints are independent, we can combine them with the log-likelihood to obtain the log-posterior, which is just given by the sum of Eqns. 18, 19 and 20, $J(x)$. Under the assumption that the log-posterior is also Gaussian, then the mean of the posterior is given by value of x that minimises J , and the *a posteriori* covariance is approximately given by the inverse of the Hessian at the minimum point (Lewis et al., 2012) 338
339
340
341
342
343
344

$$C_{post}^{-1} = H' C_{obs}^{-1} H'^T + C_{prior}^{-1} + \gamma^2 D^T D.$$

After solving for the atmospheric composition, the actual atmospheric correction can be done by applying the solved parameters to the TOA reflectance on a pixel by pixel basis. In the current version of SIAC, adjacency and terrain effects are ignored, and the surface is assumed isotropic, with no correction for BRDF effects. 345
346
347
348
349

The posterior uncertainty pertains to the atmospheric composition parameters, and not to the atmospherically-corrected surface reflectance, so the uncertainty encoded in Eq. 2.5 needs to be propagated through a re-arranged version of Eq. 16. This requires access to the partial derivatives of the different terms in Eq. 16: T_t , S and ρ_p as a function of atmospheric composition parameters. 350
351
352
353
354
355

2.6 Improving the efficiency of parameter inference 356

The minimisation of J can be performed by using efficient gradient descent algorithms such as L-BFGS-B (Byrd et al., 1995; Zhu et al., 357
358

1997). However, these are iterative methods that also require access to the gradient of J , which requires either numerical approximations or automatic differentiation of the atmospheric RT model in Eq. 18. Clearly, the computational cost of solving for atmospheric composition over an entire S2 or L8 scene, and inferring the atmospheric parameters at a spatial resolution of approximately 1km, is prohibitive. Gómez-Dans et al. (2016) uses Gaussian Process *emulators* to provide a very efficient approximation to both the 6S RT model, and to its Jacobian, and demonstrates their successful use in data assimilation problems similar to the one at hand. The availability of the approximation to the Jacobian from the emulator is also required for calculating the uncertainty in the parameters, and its propagation to surface reflectance. Emulators are also used to perform the final atmospheric correction on a per-pixel basis.

A second speed-up is obtained by performing spatial convolutions in the frequency domain. In this study, the discrete cosine transform (DCT) with a symmetric boundary conditions was used. Finally, multi-grid methods (e.g. Briggs et al. (2000)) were used to iteratively provide a more spatially refined solution. This approach greatly improves convergence rates in the current case, with a large dimensional state vector, with important correlations between parameters.

3 Study area and data

3.1 The TOA data

3.2 Sentinel 2 TOA reflectance

Sentinel 2A and Sentinel 2B were launched on 23/06/2015 and 07/03/2017 respectively. A single satellite revisits the equator every 10 days, while a constellation of two satellites achieve a equator revisit time of 5 days and 2-3 days at the mid-latitude. S2 (s) has 10 m, 20 m and 60 m spatial resolution Multi-Spectral Instrument (MSI), having 13 spectral bands ranging from 443 nm to 2190 nm.

The Landsat project keeps providing the longest temporal record of moderate resolution multi-spectral data over global earth surface. Landsat 8 was launched at 11/02/2013, having a global revisit time of 16 days in a 8 days off of Landsat 7. Two push-broom sensors: the Operational Land Imager (OLI) and the Thermal Infrared Sensor (TIRS) are mounted to provide multi-spectral and thermal observations of the earth surface at 30 m and 100 m resolution respectively. OLI has 9 spectral bands, among which band 8 is panchromatic and has a

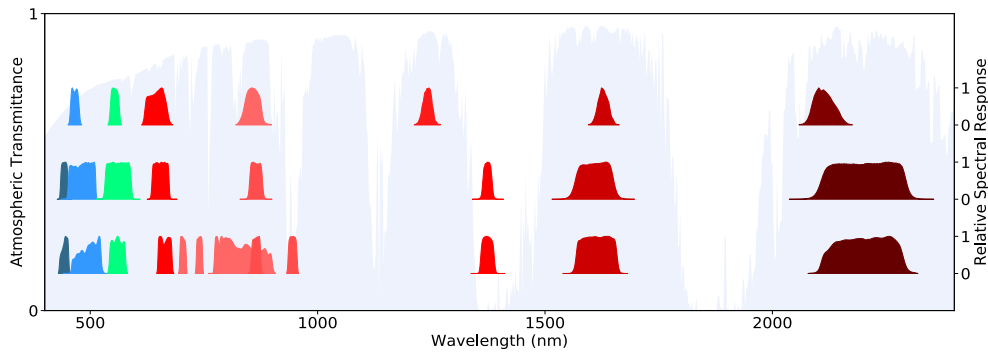


Figure 2. From the top to bottom are the MODIS, L8 and S2 relative spectral response function for each band, and the background is the atmospheric transmittance processed by 6S with MidlatitudeSummer atmosphere profile and continental aerosol model with a AOT value of 0.2 at 550 nm.

spatial resolution of 15 m. 398

In this study, we focus on the L1C Sentinel 2 products and the 399
equivalent L1C LC8 product as inputs to provide a consistent Level 2A 400
product for both sensors. Both L1C products provide a projected and 401
calibrated TOA reflectance dataset. Sentinel 2 products were obtained 402
from the Copernicus Open Access Hub , whereas the Landsat 8 403
products were obtained from the USGS. The spectral characteristics of 404
Sentinel 2 and Landsat 8 are shown in Fig. 2, whereas a description of 405
the different bands of each sensor is provided in Table 1 406

3.3 The BRDF descriptor product, MCD43 407

In this study, the surface BRDF at a coarse resolution is provided by the 408
Terra and Aqua Combined product MODIS BRDF/Albedo Model 409
Parameter Product (MCD43A1 in collection 6) (Schaaf et al., 2002; 410
C. Schaaf, 2015). This product uses the MODIS surface reflectance 411
product to fit the Ross-Thick/Li-Sparse-Reciprocal (RTLSR) linear 412
kernel models (Wanner et al., 1997; Lucht and Lewis, 2000; Roujean 413
et al., 1992; Ross, 1981; Li and Strahler, 1992). Kernel weights are 414
fitted to all good quality observations within a 16 day temporal 415
window. Observations temporally far from the center are 416
downweighted, as are those of lower quality (Wang et al., 2018). This 417
method is similar to the temporal regularisation introduced in Quaife 418
and Lewis (2010). The kernel weights ($f_{iso}, f_{vol}, f_{geo}$) can be used to 419
predict the surface directional reflectance for an arbitrary 420
view/illumination geometry given by $\Omega \Omega'$ (respectively) as 421

MODIS		Sentinel 2		Landsat 8	
Band No.	Wavelength (nm)	Band No.	Wavelength (nm)	Band No.	Wavelength (nm)
3	459-479	2	457-523	2	452-512
4	545-565	3	542-578	3	533-590
1	620-670	4	650-680	4	636-673
2	841-876	8	784-900	5	851-879
2	841-876	8A	855-875	5	851-879
6	1628-1652	11	1565-1655	6	1566-1651
7	2105-2155	12	2100-2280	7	2107-2294

Table 1. Bands in MODIS, S2 and L8, sharing similar spectral coverage as shown in Figure 2, and the spatial resolution for MODIS bands are 500 m for all the bands except red and NIR bands, *i.e.* band 1 and 2 with 250 m. S2 band 2, 3, 4 and 8 are 10 m resolution and band 8A, 11 and 12 are 20 m. L8 has 30 m spatial resolution for all the bands listed in this table.

$$\rho(\lambda_M, c) = f_{iso}(\lambda_M) + f_{vol}(\lambda_M)k_{vol}(\Omega, \Omega') + f_{geo}(\lambda_M)k_{geo}(\Omega, \Omega') \quad (21)$$

In particular, using the S2/L8 sensing viewing-illumination geometries can be used to compute the kernel values $k_{geo}(\Omega, \Omega')$ and $k_{vol}(\Omega, \Omega')$. The kernel weights f_{iso} , f_{vol} and f_{geo} are given by the MCD43A1, and using Eq. 21, one can calculate the apparent surface directional reflectance for S2 or L8, at a coarse spatial resolution and on the MODIS spectral bands.

3.4 ECMWF and AERONET

The European Centre for Medium-Range Weather Forecasts (ECMWF) produces and disseminates numerical weather predictions and global reanalysis meteorological data. In this study we use CAMS global assimilation and forecasting system [Near-real-time](#) data set, providing atmospheric composition parameters including *AOT* at 550 nm, total column water vapour and total column of Ozone as *priors*, used in this study.

The [AERONET](#) (AERosol RObotic NETwork) program is a federation of ground-based remote sensing aerosol networks and provides globally distributed observations of *AOT*, inversion products, and precipitable water. It has long been used as ground truth aerosol

measurements and used for the validation of various satellite
inversions aerosol products, and in this study we use its interpolated
AOT at 550 nm to validate the retrieved *AOT*.

4 Results

In this Section, we present results of the different stages in the
proposed atmospheric correction method.

4.1 Results of spectral mapping

The RSRs from S2, L8 and MODIS are used to simulate each sensors'
reflectance with spectra measurements from USGS Spectral Library
Version 7 DATA (Pearson et al., 2017), which contains spectra measured
with laboratory, field, and airborne spectrometer covering wavelengths
from the ultraviolet to the far infrared (0.2 μm to 200 μm). The
simulated band measurements from MODIS bands are used as bases
for the predictions of S2 and L8 bands. We use part of the spectral
library for the inversion of spectral mapping and the take the rest as
the validation sets. 6 examples of transforming from MODIS AQUA
bands to both S2 and L8 bands are shown in Fig. 3. The predictions are
well within the small error bars (calculated from Equation 7 with 95%
confidence intervals shown here). Except for 1375 nm cirrus band in S2
and L8, the MODIS predictions are very close to the measurements,
and within the 95% credible interval, suggesting that not only the
mappings are accurate, but also the uncertainty calculation is credible.
We note that the small uncertainty in the predictions appears for bands
where the source sensor either samples part of the directly, or where
there are a number of bands in the surrounding area. An example of
this not happening is the larger uncertainty in the predictions for the
band around 2200 nm. The discrepancy can be explained by the
different spectral response between MODIS and the respective S2/L8
bands in the region (see e.g. Fig. 2). This observation suggests that the
spectral mapping approach is viable if sensors have either similar or
overlapping RSR, or if a number of spectrally close bands are also
present.

In this study, both full spectrum linear models and nearest band
linear models have been developed. The latter type have been
implemented in this study as they reduce the amount of data that
needs to be used.

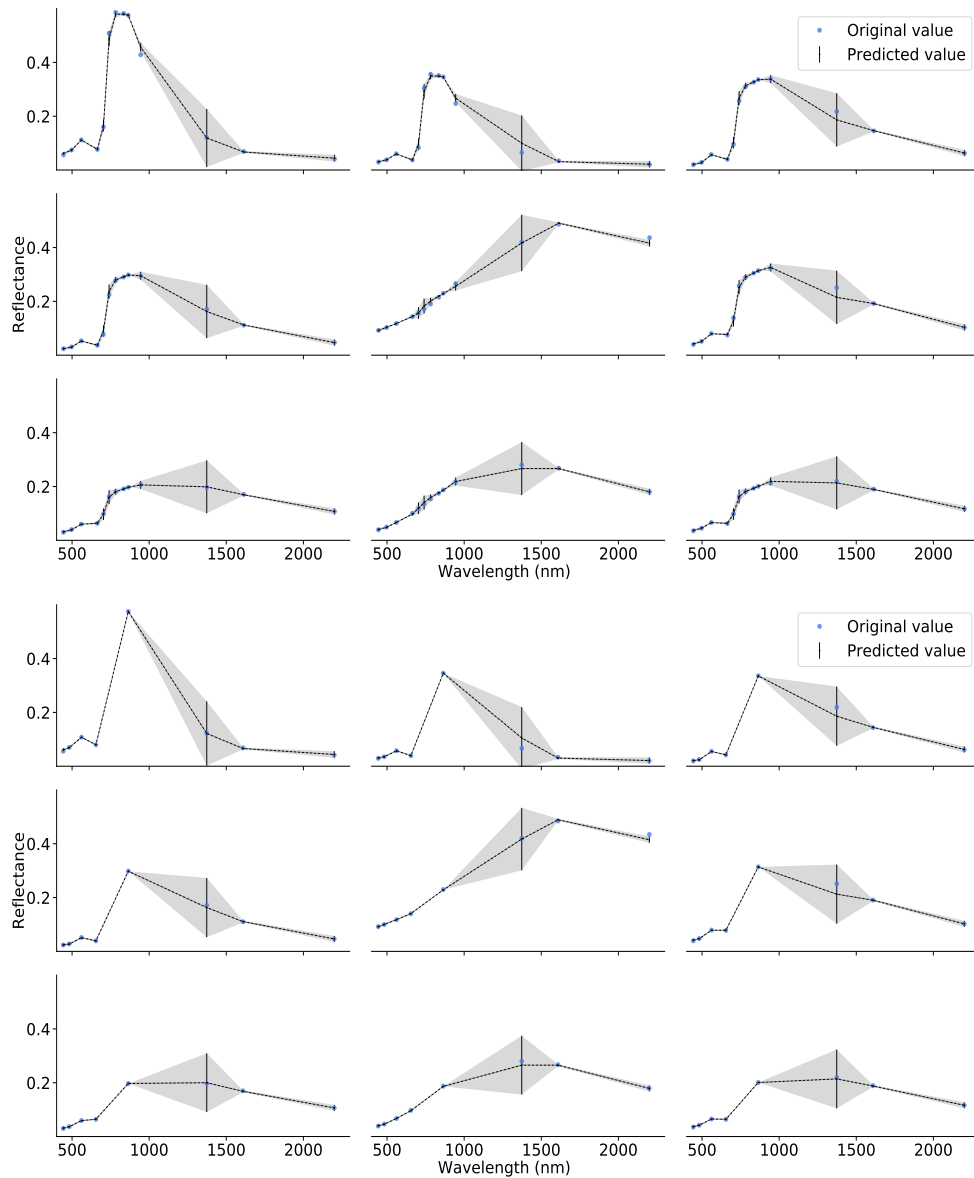


Figure 3. S2 (up) and L8 (bottom) reflectance predicted by MODIS Aqua. Predicted values are from applying the spectral mappings to the MODIS reflectance and the uncertainty is also shown with 95% confidence intervals. The original values are from the direct simulated reflectance by applying S2 and L8 RSR to the spectra. The grey areas are direct filling between neighbouring error bars.

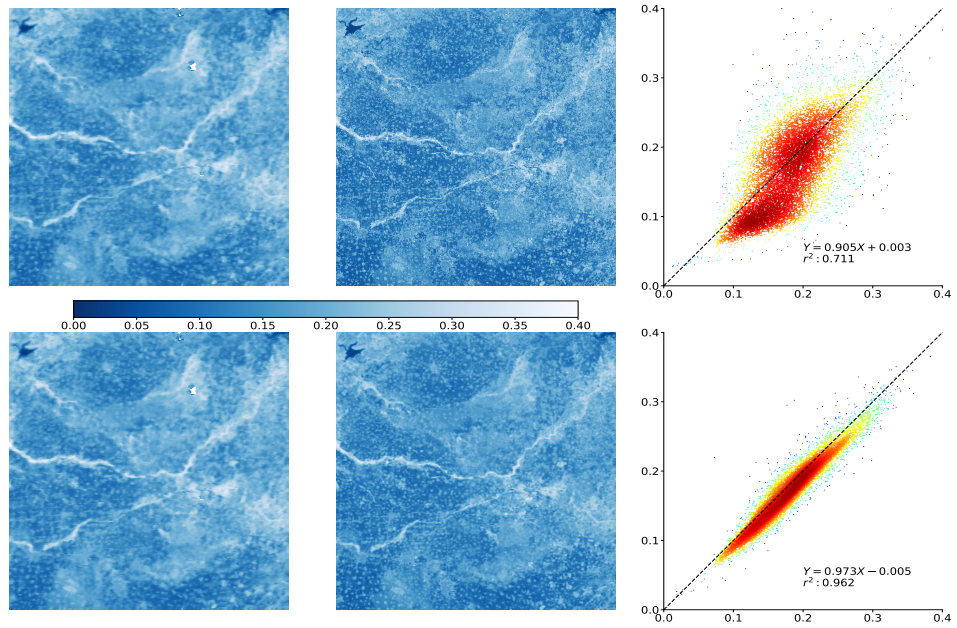


Figure 4. Comparison between MCD43 simulated surface reflectance $\rho(x_m, y_m, \lambda_{SWIR}, \Omega, \Omega')$ with $\rho_{toa_simu}(x_m, y_m, \lambda_{SWIR}, \Omega, \Omega')$, which is after the spectral mapping and PSF convolution, at SWIR band located at around 2200 nm, on 13/04/2016 S2 50SLH tile in NCP. Top row is the $\rho(x_m, y_m, \lambda_{SWIR}, \Omega, \Omega')$ and S2 TOA reflectance, with the scatter plot between the corresponding pixels (pixel's center geolocation) on the right side. Bottom row is the $\rho(x_m, y_m, \lambda_{SWIR}, \Omega, \Omega')$ with $\rho_{toa_simu}(x_m, y_m, \lambda_{SWIR}, \Omega, \Omega')$ and their scatter plot.

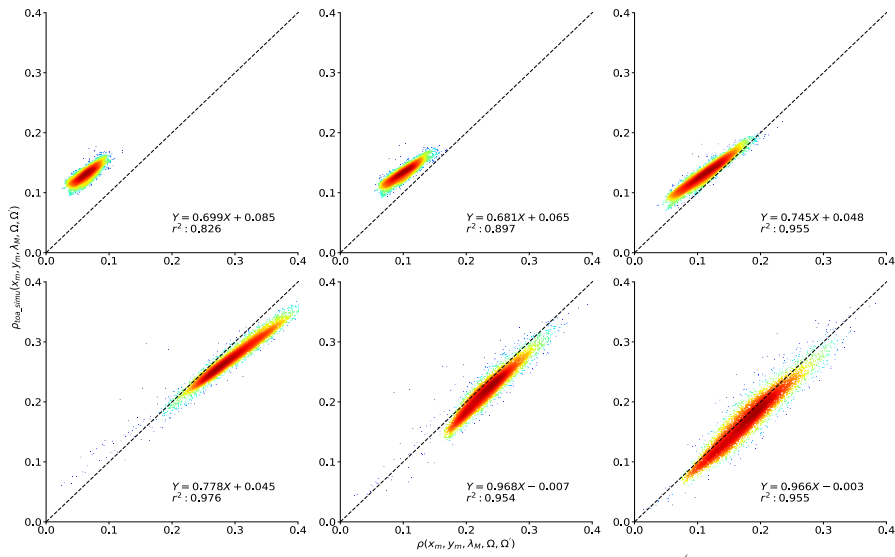


Figure 5. Per-band comparison between the $\rho(x_m, y_m, \lambda_M, \Omega, \Omega')$ and $\rho_{toa_simu}(x_m, y_m, \lambda_M, \Omega, \Omega')$ at 6 MODIS bands in Table 1, with band wavelength increasing from top-left to bottom-right.

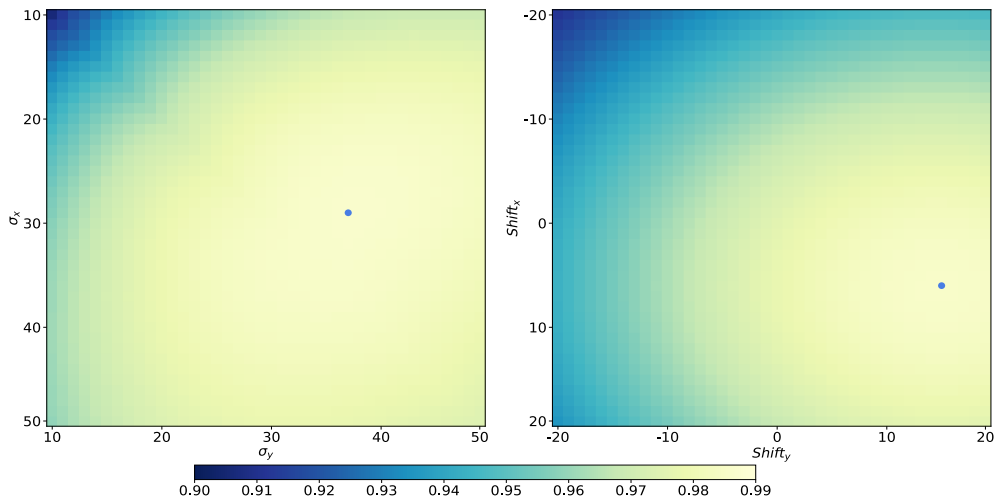


Figure 6. The correlations between $\rho(x_m, y_m, \lambda_{SWIR}, \Omega, \Omega')$ and $\rho_{toa_simu}(x_m, y_m, \lambda_{SWIR}, \Omega, \Omega')$ with different σ_x , σ_y , $Shift_x$ and $Shift_y$ values, in which the blue dots represent the largest correlation value's positions.

4.2 Results Spatial modelling (PSF)

476

We show an example of the PSF modelling in Fig. 4, where we compare the MCD43-predicted reflectance at around 2200 nm and S2 TOA reflectance over the North China Plain (S2 tile 50SLH, image acquired on April 13, 2016). The MCD43 predictions and the S2 image show broadly similar coarse patterns, with the higher resolution detail in the S2 image being clearly visible. Comparing the predicted (and spectrally transformed) reflectance from MCD43 with the S2 data pixel-by-pixel (corresponding S2 pixel at the centre of the MODIS pixel) and the PSF-convolved S2 data shows that the latter has a much stronger correlation, a slope very close to unity and a bias close to zero, indicating that modelling the spatial mismatch is a required step in combining the two datasets.

477

478

479

480

481

482

483

484

485

486

487

488

We have assumed that for a given scene, a single Gaussian PSF is required, in line with the findings of Mira et al. (2015), and we assume further that we can use the PSF derived for the 2200 nm band for all other bands.

489

490

491

492

We illustrate the effect of comparing the *ePSF*-convolved S2 TOA reflectance with the MCD43-derived BOA reflectance predictions in Fig. 5. The pattern shown there is consistent with higher atmospheric effects for the shorter wavelengths, that results both in a clear bias due to the important effect of aerosols in the intrinsic path radiance, and a slope different to unity (due to the effect of aerosols on upward and downward atmospheric transmission and spherical albedo). For the longer wavelengths after the NIR plateau, aerosol effects are less important, and the slope is close to unity and the bias close to zero, with the correlation generally being very high. Fig. 5 also provides an intuitive illustration of how the atmospheric correction scheme described in Section 2.5 works: by propagating the BOA predictions through the atmosphere, the method searches for atmospheric parameters that would result in an optimal match for all bands.

493

494

495

496

497

498

499

500

501

502

503

504

505

506

After solving for the *ePSF* parameters over a large number of S2 and L8 scenes globally, and considering the results, we note that some simplifications in the processing are feasible. A first observation is that the cost function is fairly flat around the minimum. Fig. 6 shows an example of this: for both S2 and L8, the region around the maximum correlation point has similar values (in excess of 0.98) to the maximum, suggesting that there the very accurate estimation of either the *ePSF* widths or shifts is a not very important. A second important point is that the width of the *ePSF* over a large number of scenes tends to be well defined (see Fig. 7 for an example of this): for L8, most of the vertical and horizontal shifts lie respectively between 10 and 17 and 7 and 15 pixels. For S2, these numbers are similar, only that in this case,

507

508

509

510

511

512

513

514

515

516

517

518

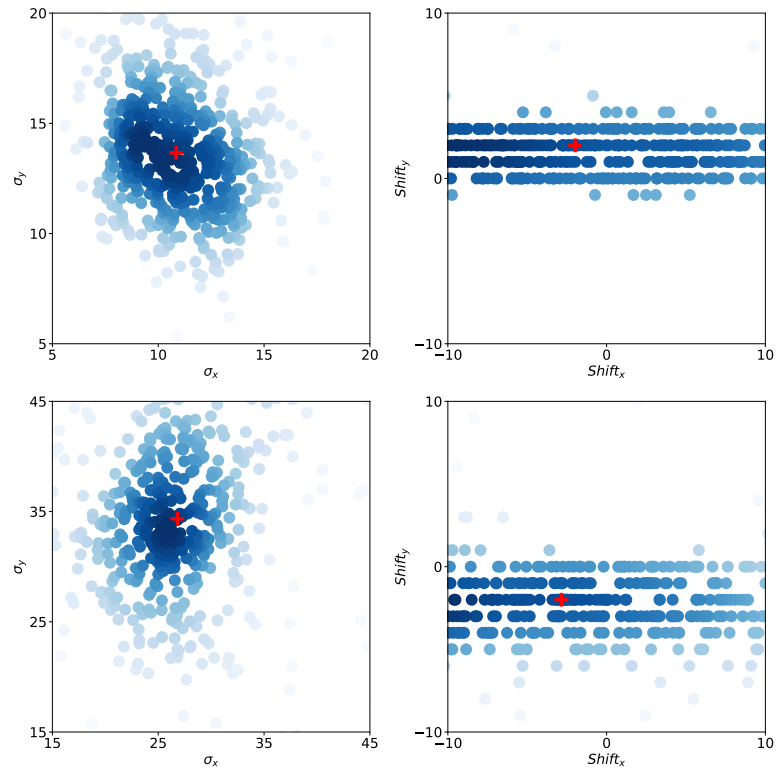


Figure 7. The density scatter plots of solved PSF parameters, σ (left) and *Shift* (right) in x and y direction for L8 (top row) and S2 (bottom row), where the red markers stands for the median of those parameters.

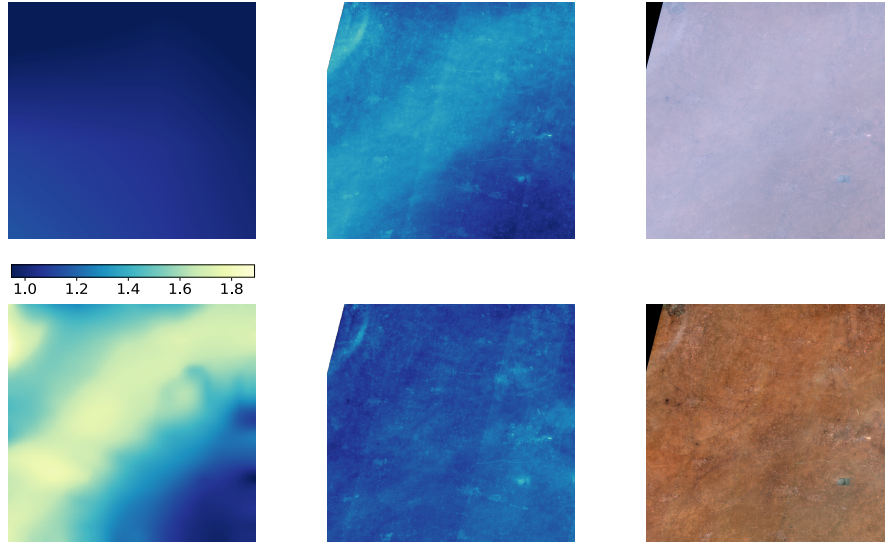


Figure 8. The *prior* and *posterior* AOT over S2 50SMH on 10/02/2016 and their shared colorbar are in the first column. Figures in the second column are the log transformed band 1 TOA and surface reflectance, while the TOA and BOA RGB images are shown in the third column for the same tile over the same time.

the number of pixels is three times larger to account for the higher spatial resolution of S2. The shift, however, appears more scene-dependent, and also have a larger influence on the correlation cost function.

The points made above suggest that a fixed value of σ_x and σ_y may be used for all images, but that still the effect of the pixel shift needs to be inferred on a scene by scene basis. We have not said much of rotation angle θ (introduced in Eq. 10). In the studied cases, its value is around $\pm 8^\circ$, and its effect can be effectively compensated by $Shift_{x,y}$. In order to reduce the computational burden of calculating the $ePSF$ parameters, we have taken the median shifts as a reference, assumed the rotation angle to be 0° , and only solved for $Shift_{x,y}$ on a scene basis.

4.3 Results Atmospheric parameters inversion

In this Section, we illustrate the proposed method working on inferring atmospheric composition parameters. Due to S2 and L8 having bands outside from the strong O_3 absorption region, TCO_3 is taken from CAMS, and only AOT and TCWV are inferred from the data. Fig. 8 shows a demonstration of the procedure. Here, an image captured over the North China Plain (tile 50SMH) by S2 on 10 February 2016 has been processed. The CAMS prior mean in Fig. 8 is around 1, and approximately constant over the scene. The TOA reflectance for band 1

of the S2 sensor (shown in log transformed units to enhance the dynamic range) shows two clear high aerosol bands. The true colour TOA image shows a very strong atmospheric effect, consistent with the expectation of high AOT.

The retrieved AOT (bottom left panel in Fig. 8) shows a marked departure from the prior value. Two very high aerosol bands are clearly resolved, consistent with the TOA reflectance image. The result of applying the atmospheric correction results in an important reduction of the atmospheric effects, particularly evident from the BOA true colour composite (bottom right panel of Fig. 8).

Some artefacts are also apparent. In the bottom right corner of the scene, the AOT map reverts to the prior value from CAMS, which results in a poorer correction of the atmospheric effects. This is caused by lack of high quality MCD43 retrievals in this area at this time, which results in the AOT estimate being strongly driven by the prior from CAMS, as well as some spatial diffusive effects from areas where the algorithm performs well. A second artefact are some visible stripes (visible in the middle top and bottom panels). These are caused by the combinations of observations from different detectors (Pahlevan et al., 2017), and have no relationship with the atmospheric correction method. It is also worth noting that when solving for the *ePSF* parameters for this scene, the optimal linear correlation was only around 0.55, but clearly, the system is still able to produce reasonable results in this challenging environment.

We note that the scene shown in Fig. 8 is a particularly challenging one: at this time of the year, most of the soil is bare, and aerosol loading is very high. In these circumstances, atmospheric methods relying on dark dense vegetation would perform poorly.

As a further illustration of the approach on Sentinel 2 data, we show similar visualisations of AOT and TCWV priors, the associated posteriors, as well as TOA and BOA blue band reflectance, as well as TOA and BOA true colour composites for a number of different sites spanning the globe in Fig. 9 (Zvenigorod), Fig. 10 (Yuma), Fig. 11 (Manaus-EMBRAPA), Fig. 12 (Jaipur) and Fig. 13 (Rome). While the effect of the atmospheric correction is evident in all these cases, it is important to note that the prior mean is significantly updated when the posterior mean of both AOT and TCWV are calculated. Spatial patterns are clearly visible in all the examples for both parameters, and in many cases, the average value from CAMS changes substantially when the proposed method is deployed. While this is expected for AOT, it is remarkable that the spatial patterns are visible for TCWV even when the 940 nm band has not been used.

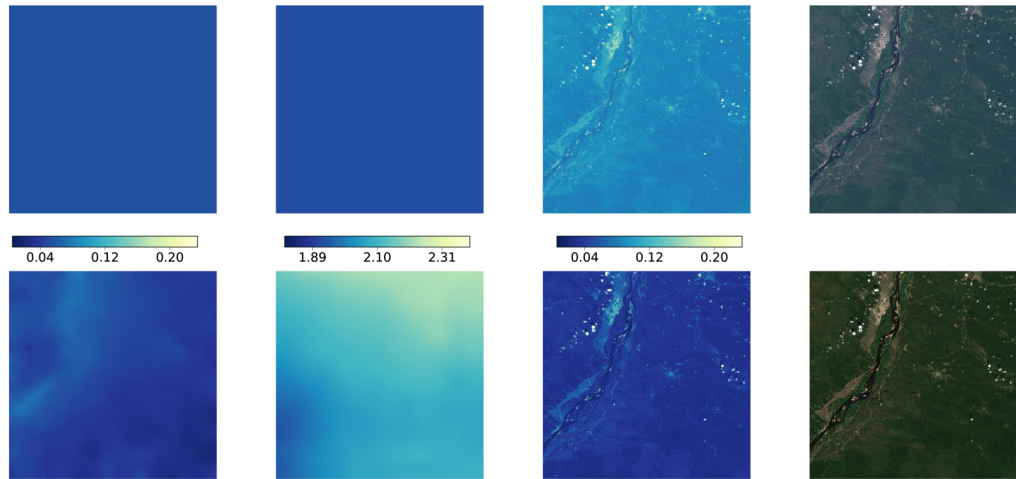


Figure 9. Example of retrieval on S2 data over Zvenigorod site (S2 Tile 37UCB, 24 Jul 2017). (Top row, left to right): AOT prior mean from CAMS, TCWV prior mean from CAMS, blue band TOA reflectance, TOA RGB composite (Bottom row, left to right): *A posteriori* AOT mean, *A posteriori* TCWV mean, blue band BOA reflectance, BOA RGB composite.

5 Validation

582

We have made an attempt to validate the proposed atmospheric correction method. Since the SIAC procedure proceeds by first inferring AOT and TCWV, and then using these to correct the TOA reflectance, we show comparisons with *in situ* AOT and TCWV measurements from the AERONET network, as well as actual comparisons of retrieved surface reflectance with *in situ* measurements collected by the RadCalNet team.

583

584

585

586

587

588

589

5.1 Validation of atmospheric composition

590

For the AOT and TCWV validation, 323 simultaneous (within at most one hour of each other) acquisitions from S2 and L8 were selected globally. These acquisitions were also taken over AERONET sites to provide a reference comparison. AERONET measurements are temporally interpolated to get an estimate of AOT at the time of satellite overpass. In order to estimate the *in situ* AOT at 550 nm, the AERONET spectral log-transformed data were interpolated using a second order polynomial between 400 nm and 860 nm.

591

592

593

594

595

596

597

598

Results of the comparisons are shown in Fig. 14 for AOT and Fig. 15 for TCWV. In terms of AOT retrievals, the results for S2 appear to be good, with most of the match-up estimates encompassing the *in situ*

599

600

601

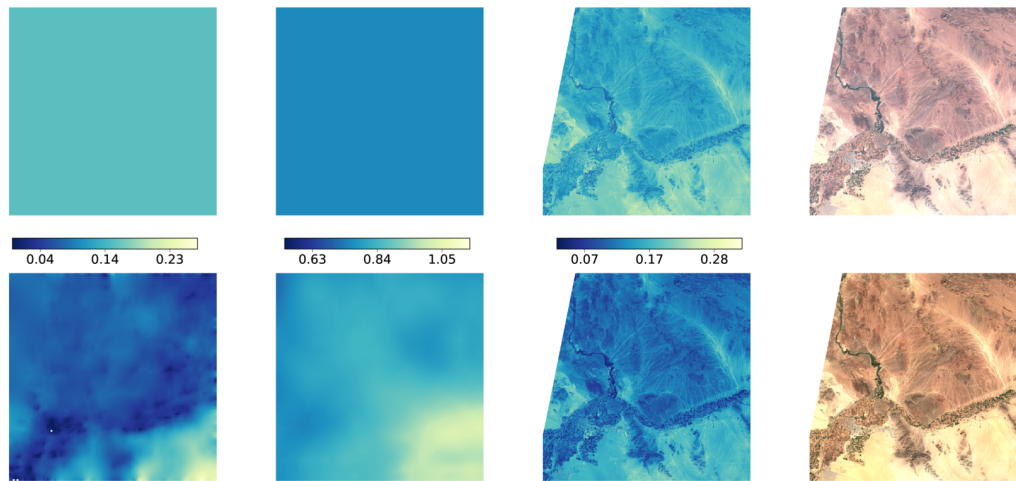


Figure 10. Example retrieval over Yuma site (S2 tile 11SQS, 10 Oct 2017). Panels as in Fig. 9

value within their uncertainty (98%, or 316 out of 323, of the *in situ* AOT estimates are within the 1.96σ span of the retrievals, compared with a theoretical 97.5%). The correlation is very high (coefficient of determination $r^2 > 0.9$), and while the slope is slightly below unity (0.92), the bias is close to 0 (0.01). The root mean squared error (RMSE) is also small: 0.022. The underestimation in AOT occurs for low AOT values, which will have a limited impact in the retrieved surface reflectance.

Results from L8 retrievals of AOT are similar to S2, but the underestimation of AOT is slightly higher than for S2 (slope of linear fit 0.84), but the other statistics suggest a similar pattern.

The outliers (depicted in blue in Fig. 14) for moderate to high AOT values (e.g. $AOT \leq 0.5$) were mostly caused by biomass burning events, or by dust events at the overpass time. The spectral properties of these aerosol species are quite different to the continental aerosol model that is assumed in SIAC, and thus result in poor retrievals. Outliers in the low AOT region were generally due to poor quality BRDF characterisation in the MCD43 product. This would also be the case for situations where there are rapid changes in the surface (e.g. snow/thaw). For similar reasons, the algorithm will work poorly in lakes and inland waters, although the use of a prior and spatial smoothing constraints may provide an adequate estimation of AOT over small water bodies.

In Fig. 15, the *in situ* measurements of TCWV are compared with the SIAC retrievals for S2 and L8. Although there is a lot of scatter, this partly due to the uncertainty of the *in situ* dataset: Pérez-Ramírez et al.

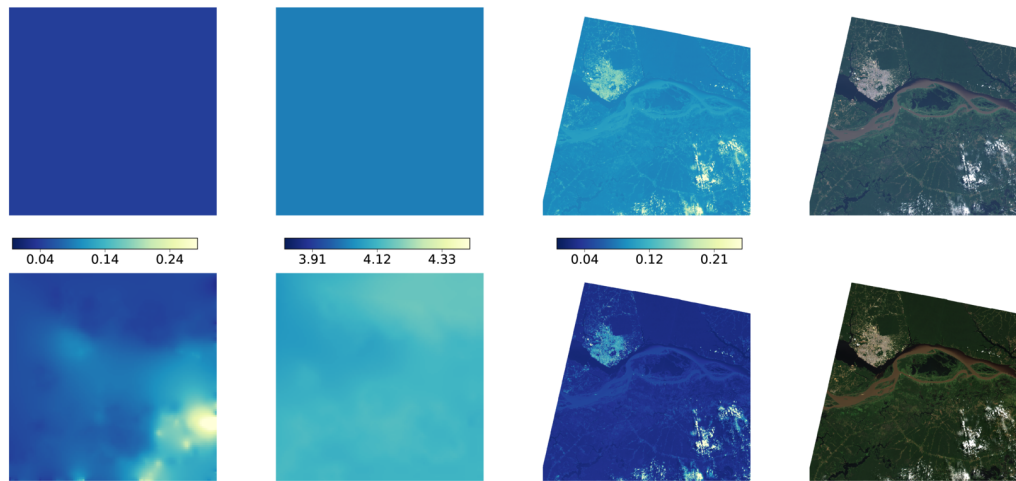


Figure 11. Example retrieval over Manaus-EMBRAPA site (S2 tile 20MRB, 27 Jul 2016). Panels as in Fig. 9

(2014) suggests that there is a 15% uncertainty in AERONET TCWV estimates. The general statistics show surprisingly good results, with a strong correlation (coefficient of determination better than 0.96 for both L8 and S2), a slope very close to unity (0.98 and 0.97 for S2 and L8, respectively), and a small bias (0.19 and 0.09 for S2 and L8, respectively). This result is even more remarkable as for S2 the 940 nm band, designed precisely for water vapour estimation has not been used. This good results suggest good correction of water vapour effects over the infrared spectral region.

5.2 Validation of surface reflectance

The previous Section suggests that the retrieval of atmospheric composition in SIAC is succesful. The goal of SIAC is however to perform consistent atmospheric correction across different sensors. In this Section, we attempt to provide an assessment of the performance of atmospheric correction of S2 and L8 data.

The S2 and L8 scenes used in Section 4.3 were atmospherically corrected. These data were collected within one hour of each other, and surface reflectance in overlapping spectral regions in both sensors should be highly correlated. Differences in spatial coverage, acquisition geometry, spectral sampling and other sensor characteristics will somehow impact this comparison, but the effect should be small. Pixels in the corresponding 323 S2 and L8 scenes presented in Section 4.3 that overlap spatially were selected. In order to account for the different spatial resolutions, the 10 m S2 bands were spatially

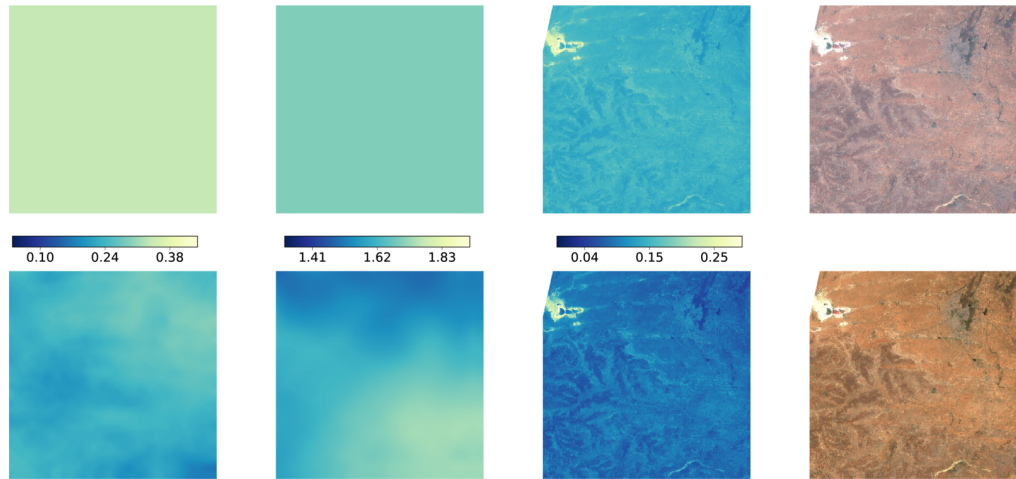


Figure 12. Example retrieval over Jaipur site (S2 tile 43REK, 22 Oct 2017). Panels as in Fig. 9

averaged and reprojected to the L8 30 m grid. The 20 m S2 were
interpolated to the L8 grid using bilinear interpolation. In this dataset,
pixels that had reflectance differences between sensors larger than 0.05
(blue band) or 0.1 (all other bands) were discarded, as these errors
could be caused by other effects other than atmospheric correction (e.g.
cloud, cloud shadow, landscape heterogeneity, ...). This filter only
removes a small fraction of the total pixels, as 99.5% of the pixels
remain in the dataset, with the total number of pixels available for
direct comparison of the order of $10^6 - 10^7$.

The comparison between S2 and L8 surface reflectance is shown in
Fig. 16 as a two-dimensional histogram. Clearly, the reflectances are
highly correlated (coefficient of determination $r^2 > 0.95$ for all bands,
and $r^2 > 0.98$ for bands in the NIR and SWIR regions), with a small
RMSE ($RMSE < 10^{-4}$). The bias is very small (less than 0.001 for all
bands), and the slope is between 0.91 (blue band) and 1.04 (NIR band).
All these diagnostics suggest that after atmospheric correction, the
surface reflectances from both sensors are consistent, barring spatial
heterogeneity effects. The lower slope for the blue band might be
caused by differences in AOT retrieval between both sensors: the slope
of the retrieved AOT for Landsat is lower than that of S2 (see Fig. 14,
which would appear as a relative AOT under-correction for L8 with
respect to Landsat. The effect would be larger in the blue bands.

The comparisons above suggest that the surface reflectances are
consistent between both sensors. However, the surface reflectances
have not been compared with any standard. Recently, the Working
Group on Calibration and Validation (WGCV) of the Committee on

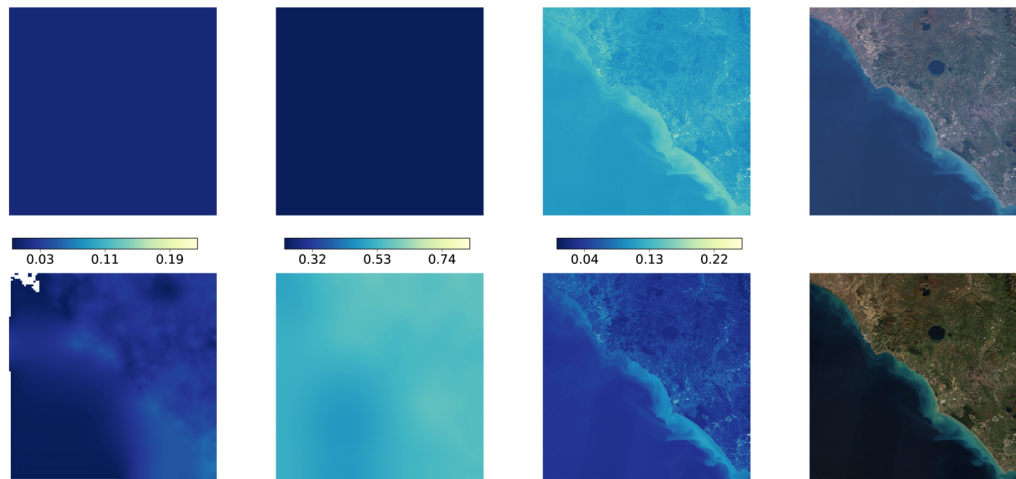


Figure 13. Example retrieval over Rome site (S2 tile 32TQM, 27 Nov 2017). Panels as in Fig. 9

Earth Observation Satellites (CEOS) has started providing ground surface reflectance data through the Radiometric Calibration Network portal (RadCalNet,). RadCalNet provides nadir-view, top-of-atmosphere reflectance at 30 minute intervals from 9am to 3pm local standard time at 10 nm intervals from 400 nm to 2500 nm, which is calculated from ground nadir-view reflectance measurements, and atmospheric measurements such as surface pressure, columnar water vapour, columnar ozone, aerosol optical depth and the Angstrom coefficient. TOA reflectance is simulated by propagating the measured surface reflectance through the atmosphere using the MODTRAN radiative transfer model, parameterised by local atmospheric composition measurements

The RadCalNet data can thus be used as a comparison for the SIAC-corrected S2 and L8 scenes. To do this, the sensor spectral response functions are applied to the RadCalNet surface reflectances which are temporally closest to the S2 and L8 acquisition times, and a direct comparison can be performed. Use of the RadCalNet top-of-atmosphere reflectance is also used as a diagnostic tool: if the sensor TOA reflectances do not match the RadCalNet reflectances, then any mismatch observed in the surface reflectance comparisons might not be attributable to the atmospheric correction, but rather to other issues.

We have compared the SIAC-corrected data with measurements from three RadCalNet sites: the ESA/CNES site in Gobabeb (Namibia), the CNES site in La Crau (France) and the University of Arizona's site at Railroad Playa Valley (Nevada, United States), as these three sites

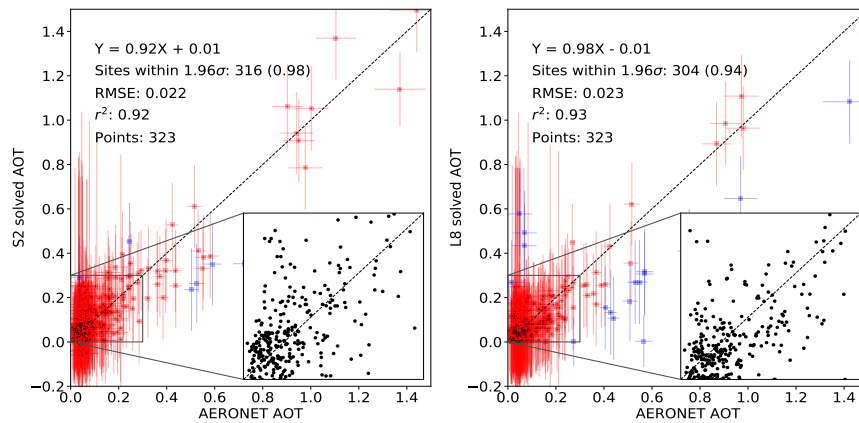


Figure 14. The retrieved AOT values against AERONET measurements from S2 (left) and L8 (right) over the same 323 sites, where the vertical lines of each point is the uncertainty of solved AOT values and the horizontal error bars are from the interpolation of 5% and 8% between 0.05 to 1.5 according AERONET validation reports. On both panels, the inset plot shows the region region marked by the black square in more detail, with $0 \leq AOT \leq 0.3$.

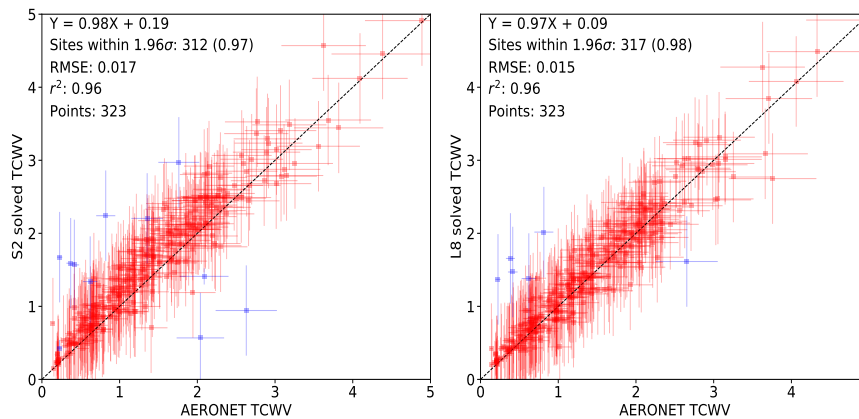


Figure 15. The retrieved TCWV values against AERONET measurements from S2 (left) and L8 (right) over the same 323 sites, where the vertical lines of each point is the uncertainty of solved TCWV values and the horizontal error bars are 15% of AERONET TCWV values.

measure over the entire solar reflective spectrum. Railroad Playa Valley is a high-desert playa surrounded by mountains to the East and West, La Crau has a thin pebbly soil with sparse vegetation cover, and Gobabeb is over gravel plains. Results of the comparisons are shown in Figs. 17, 18 and 20, with the comparison results summarised in Table 2. Generally speaking, the agreement between the SIAC-retrieved surface reflectance and the reference measurements is high on the three sites, with RMSEs values for the BOA products of around 0.5-0.7% reflectance (Gobabeb), 0.6-1% (La Crau) and around 2% for Railroad Valley Playa. We note that RMSE values for the TOA comparisons are of the same order per site, although slightly larger, suggesting that the atmospheric correction performed by SIAC is comparable to the atmospheric modelling done with the RadCalNet data. The best performance is found over Gobabeb, with the La Crau exhibiting a large temporal variability, while Railroad Playa Valley shows an important mismatch for the TOA measurements already. In general terms, the *in situ* measurements fall within the uncertainty estimates given by SIAC, and these uncertainties are particularly large in the S2 atmospheric correction bands (band 9 for water absorption and band 10 for cirrus). As there is a strong sensitivity to atmospheric composition, the uncertainty on these bands is quite high, and they have been left out of the atmospheric composition statistics. It is important to point out that in all three cases, SIAC does a particularly good job at retrieving the blue and deep-blue bands, which would be the spectral areas with the highest impact of aerosols, strongly suggesting that SIAC is doing a good atmospheric correction. This is very significant, as two of the sites are located in arid regions, where finding reference points for atmospheric correction methods based on e.g. dark dense vegetation might not be feasible.

6 Discussion

The previous sections have introduced the SIAC concept, and shown some initial validation results. The results show that the proposed method results in accurate retrievals of uncertainty-quantified land surface reflectance, both for S2 and L8. Comparisons with sun photometer data suggest that the SIAC processing chain can accurately retrieve AOT and TCWV from both S2 and L8 data, and that propagating these estimates to surface reflectance results in data comparable with *in situ* surface reflectance measurements. Moreover, the surface reflectances for the two sensors appear to be compatible, an important step in using these sensors together for land monitoring applications. A number of important issues are worth discussing.

RadCalNet Site	Measurement	Sensor	Slope	Intercept	RMSE	R^2
Gobabeb	TOA	S2	1.0454	-0.0157	0.0072	0.9903
Gobabeb	BOA	S2	0.9967	-0.0052	0.0049	0.9950
Gobabeb	TOA	L8	1.0512	-0.0149	0.0103	0.9950
Gobabeb	BOA	L8	1.0510	-0.0188	0.0070	0.9970
La Crau	TOA	S2	0.9188	0.0143	0.0088	0.9697
La Crau	BOA	S2	0.9136	0.0117	0.0065	0.9832
La Crau	TOA	L8	0.9139	0.0141	0.0163	0.9745
La Crau	BOA	L8	0.9173	0.0097	0.0130	0.9837
Railroad Valley Playa	TOA	S2	1.0982	-0.0217	0.0276	0.9236
Railroad Valley Playa	BOA	S2	1.0536	-0.0143	0.0225	0.9428
Railroad Valley Playa	TOA	L8	1.0771	-0.0226	0.0271	0.9834
Railroad Valley Playa	BOA	L8	1.1123	-0.0378	0.0213	0.9902

Table 2. Results of comparisons between top-of-atmosphere and bottom-of-atmosphere satellite products and contemporary RadCal-Net measurements on the same spectral bands.

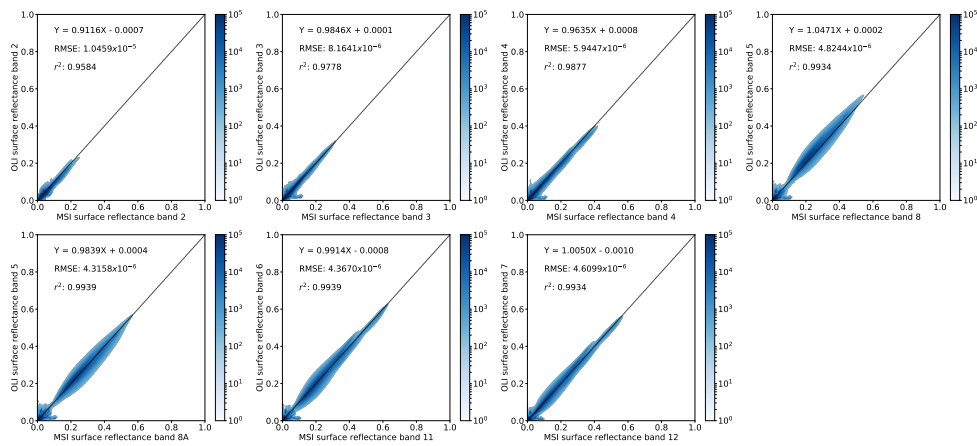
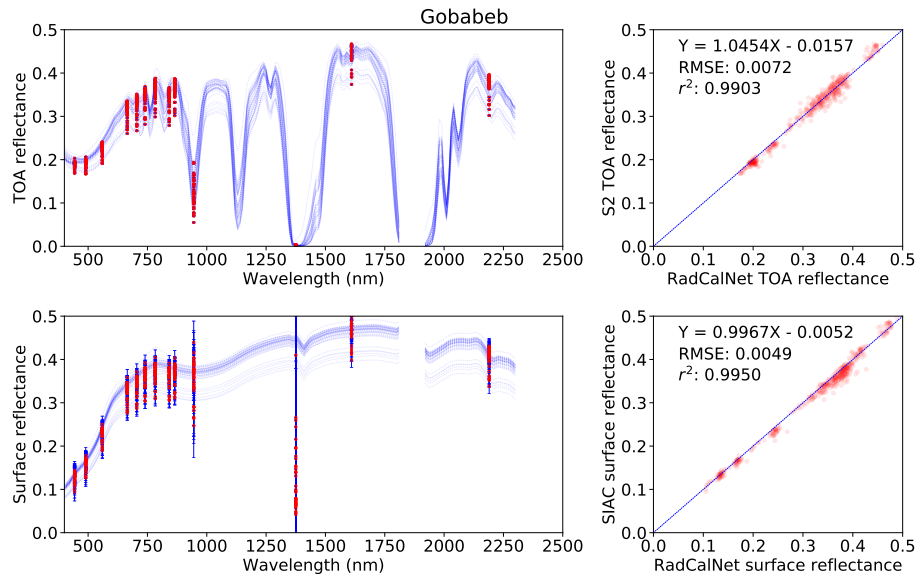
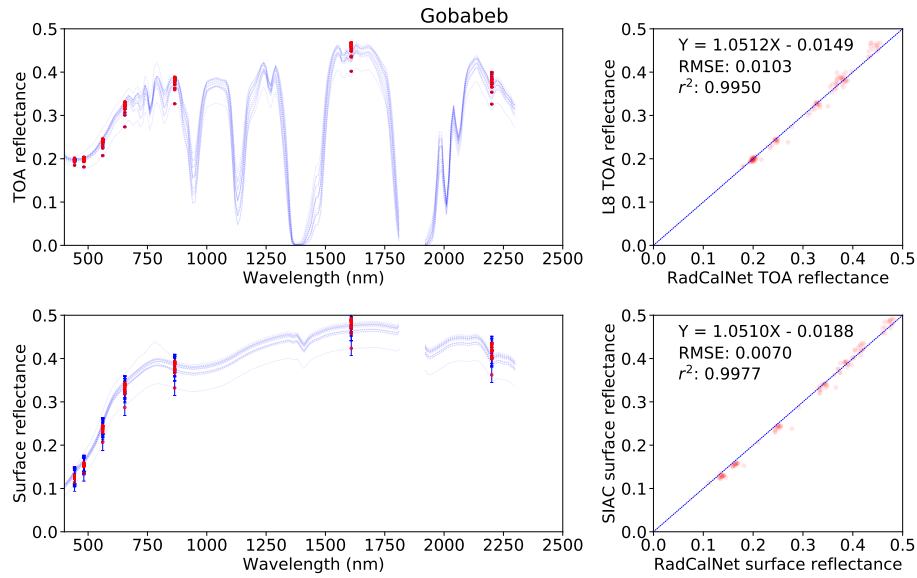


Figure 16. 2D histogram of surface reflectance after the atmospheric correction from 323 S2 and 323 tiles overlapping area, and each subplots shows the results for the closest S2 and L8 bands. The colourbar is shown using a logarithmic scale.

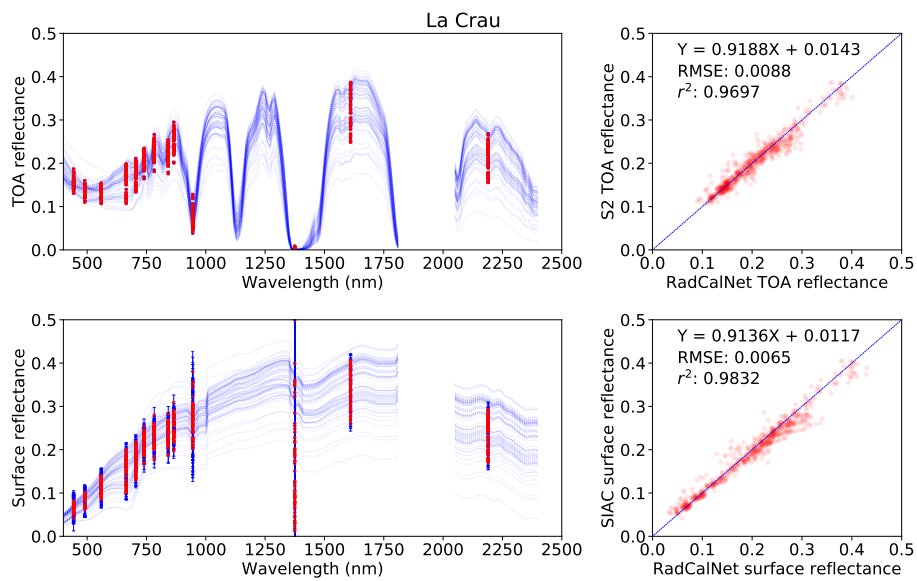


(a) Sentinel 2

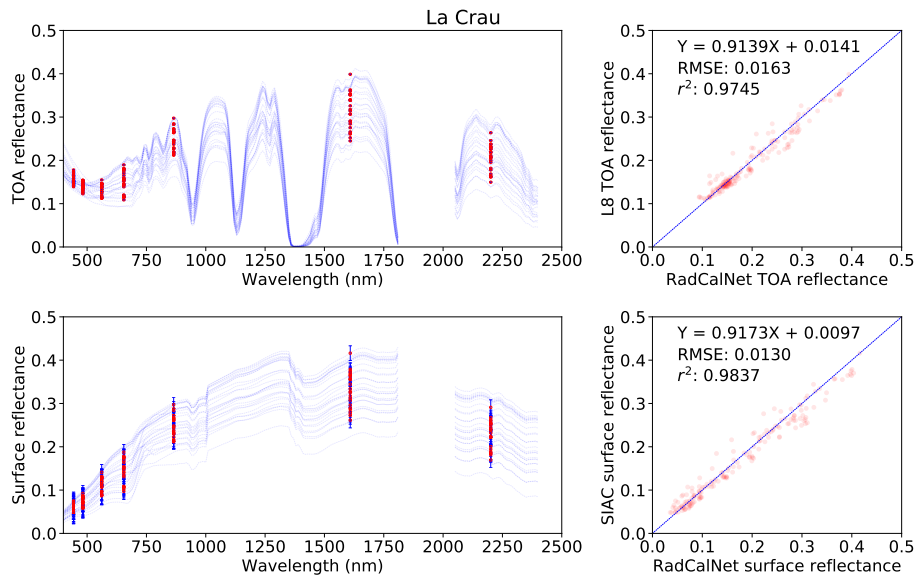


(b) Landsat 8

Figure 17. Comparison between the S2 (top) and L8 (bottom) TOA reflectance and RadCalNet simulated nadir-view TOA reflectance (top row), and the surface reflectance after correction against RadCalNet nadir-view surface reflectance (bottom row) at Gobabeb. The blue lines at left are different spectra measurement from RadCalNet and the red dot with blue error bars are the TOA or surface reflectance and TOA reflectance with uncertainty.

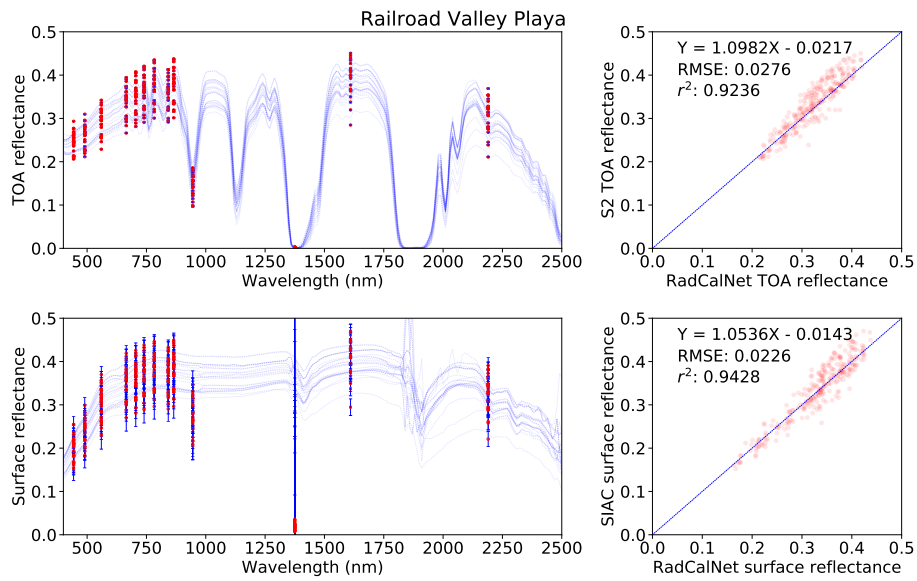


(a) Sentinel-2



(b) Landsat 8

Figure 18. Same as Fig. 17 but for La Crau site.



(a) Sentinel 2

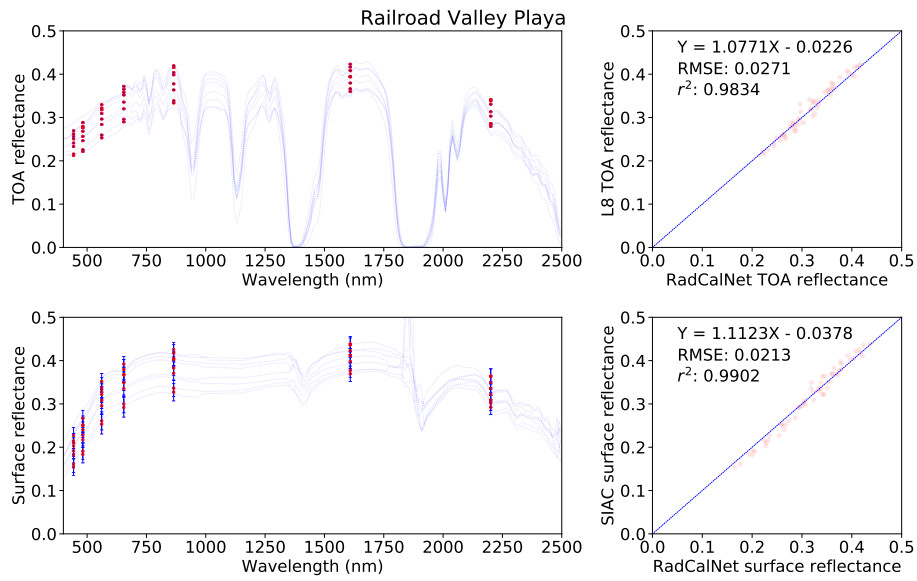


Figure 19. Landsat 8

Figure 20. Same as Fig. 17 but for Railroad Valley Playa site.

While a lot of effort has gone in propagating the uncertainty through SIAC, the system relies on a single value of at sensor uncertainty for the L1C, identical for both L8 and S2. While efforts to provide credible figures for the L1C product have been made for S2 (Gorroño et al., 2017, 2018), these are yet to be incorporated into SIAC. Similar efforts in understanding the L1C uncertainty in measured reflectance for L8 are necessary to produce adequate estimates of uncertainty for this sensor.

As the goal of this study was to demonstrate the system for both L8 and S2, special features from Sentinel 2 have not been relied on. For example, band 10 in Sentinel 2 can be used to accurately infer TCWV such as atmospheric pre-corrected differential absorption technique from Schläpfer et al. (1998) can be readily used. These estimates could then be used as a prior pdf in addition to the CAMS prior (ensuring that the used bands are removed from further correction). Similarly, other sources of information can be easily added to the system as priors without changing the internal functioning of SIAC.

SIAC relies on the expectation of surface reflectance provided by the MODIS MCD43 product. This works well, but a number of limitations exist. Firstly, the lack of a per-pixel uncertainty in the kernel weights stored in the MCD43 product only provides a rough indication of pixel quality, and a more credible uncertainty on the product would result in better product uncertainty. Second, the MCD43 product uses an exponentially weighted combination of observations acquired over 16 days. This can lead to gaps due to lack of observations, which can result in not enough surface reference samples being available. Ways around this might be to fill in these gaps with a BRDF climatology, such as the one produced by the ESA-funded GlobAlbedo project (<http://www.globalbedo.org>), or to perform simple temporal gap filling. This latter approach has been implemented in SIAC. Another complication is that the windowed nature of MCD43 may result in over smoothing of fast changes in the land surface (e.g. snow thawing, crop harvesting, fires, ...). If either gaps or fast changing regions are spatially confined to a small region, the use of the CAMS prior and spatial regularisation should counteract their effect. A more co-ordinated approach would aim to provide a global dataset of BRDF parameters using observations from other coarse resolution sensors, in addition to MODIS: VIIRS, Sentinel3/OLCI, Sentinel3/SLSTR, etc.

In this study, the atmospheric composition is set by a model (6S in this case), and by a choice of aerosol optical properties (continental aerosol model). The use of emulators of the RT model makes it easy to change the RT model entirely, or to use a different configuration of the currently used model. It may also be possible to modify SIAC to

retrieve independent aerosol species concentrations by both modifying the RT model (and thus extending the number of parameters that go in the inference), and by using data on species distribution available from CAMS and extending the prior to cover these. A similar approach has been implemented in the MAJA processor (Rouquié et al., 2017), which uses the CAMS aerosol species data to define the aerosol types for the atmospheric correction, and has found improved atmospheric correction results over deserts. This approach may well be valuable in areas of high dust aerosol loading, or in situations where biomass burning results in an important contribution to aerosol concentrations.

The method outlined in this study has been applied and demonstrated on S2 and L8 data. The method is, however, general, and can be readily extended to other sensors. The information required in order to adapt SIAC to work with these sensors is basic: spectral response functions, uncertainty of the L1C product, and standard metadata such as view/acquisition geometries. The method could be easily extended to other satellites from the Landsat family (LT5 and ETM+, for example), but due to the reliance on MCD43, only for acquisitions within the MODIS era. The code can also be extended to work on coarse resolution sensors, such as Sentinel3/OLCI or Proba-V.

A number of further refinements are planned to be added to SIAC. These include: dealing with the so-called adjacency effect (Ouaidrari and Vermote, 1999; Lyapustin and Kaufman, 2001), topographic effects (e.g. methods such as the one introduced by Shepherd and Dymond (2003) might be employed) and BRDF normalisation (Roy et al., 2016).

Finally, it is worth noting that the use of an expectation of surface reflectance at coarse resolution might provide a way to detect clouds and cloud shadows at a coarse scale. Cloud and cloud shadow masking have not been considered yet as part of SIAC.

7 Conclusions

We introduce the SIAC method for atmospheric correction. This method provides a consistent atmospheric correction for different sensors, resulting in uncertainty-quantified land surface reflectance. In this study, we illustrate its use with Sentinel 2 and Landsat 8 data. The main differences between SIAC and other atmospheric correction approaches are to be found in the use of an expectation of surface reflectance at coarse resolution (in this case, coming from the MODIS MCD43 BRDF kernels product, but not limited to this product), the use of the Copernicus Atmosphere Monitoring Service (CAMS) data as a prior constraint, the use of spatial regularisation in atmospheric composition parameters, and the use of state of the art atmospheric

radiative transfer models through Gaussian Process emulators 829
[Gómez-Dans et al. \(2016\)](#). The coarse and high spatial resolution data 830
are made comparable by modelling an effective point spread function 831
(PSF) directly from the data, and by using a set of simple linear spectral 832
transforms. 833

We have validated both retrieved atmospheric parameters and 834
surface reflectance with *in situ* estimates. Aerosol Optical Thickness 835
(AOT) retrieval for both S2 and L8 shows a very high correlation to 836
AERONET estimates ($r^2 > 0.9$, $RMSE < 0.025$ for both sensors), 837
although with a small underestimate of AOT. Total Columnar Water 838
Vapour (TCWV) is accurately retrieved from both sensors 839
($r^2 > 0.95$, $RMSE < 0.02$), and in the case of Sentinel-2, without using 840
data from the 940 nm band. 841

Comparisons with *in situ* surface reflectance measurements from the 842
RadCalNet network show that SIAC is able to provide accurate 843
estimates of surface reflectance across the entire spectrum, with $RMSE$ 844
mismatches with the reference data between 0.005 and 0.02 in units of 845
reflectance, both for Sentinel 2 and Landsat 8. 846

For near-simultaneous Sentinel-2 and Landsat-8 acquisitions, there 847
is a very tight relationship between surface reflectance acquired from 848
both sensors, with no clear biases. 849

All in all, the SIAC approach is a generic approach to accurate 850
atmospheric correction from heterogeneous sensors. The proposed 851
method paves the way for the combined use of surface reflectance from 852
different sensors, being a critical step in realising the concept of a 853
"virtual constellation" of satellites. The approach for uncertainty 854
quantification is based on standard error propagation, and takes into 855
account instrument uncertainty, prior uncertainty as well as the 856
sensitivity of the radiative transfer model used in the atmospheric 857
correction. 858

The code for SIAC is written in Python, and is released under the 859
GPLv3 open source licence. The code can be obtained from 860
<https://github.com/marcyin/SIAC>. 861

Acknowledgements 862

The authors would like to acknowledge financial support from the 863
European Unions Horizon 2020 research and innovation programme 864
under grant agreement No 687320 MULTIPLY (MULTIscale SENTINEL 865
land surface information retrieval Platform), and from the European 866
Space Agency (ESA) under Contract 4000112388/14/I-NB SEOM 867
SY-4Sci Synergy. JGD and PL were supported by the Natural 868
Environment Research Council's (NERC) National Centre for Earth 869

Observation (NCEO). PL was supported by STFC China project number 870
533651. 871

References

- Briggs, W. L., Henson, V. E., and McCormick, S. F. (2000). *A Multigrid Tutorial, Second Edition*. Society for Industrial and Applied Mathematics. 872
873
874
875
- Byrd, R. H., Lu, P., Nocedal, J., and Zhu, C. (1995). A limited memory algorithm for bound constrained optimization. *SIAM Journal on Scientific Computing*, 16(5):1190–1208. 876
877
878
- C. Schaaf, Z. W. (2015). Mcd43a4 modis/terra+aqua brdf/albedo nadir brdf adjusted refdaily l3 global - 500m v006. 879
880
- Capderou, M. (2005). *Satellites: Orbits and Missions*. Springer. 881
- CEOS (2013). Ceos virtual constellations. 882
- Chavez, P. S. et al. (1996). Image-based atmospheric corrections-revisited and improved. *Photogrammetric engineering and remote sensing*, 62(9):1025–1035. 883
884
885
- Doxani, G., Vermote, E., Roger, J.-C., Gascon, F., Adriaensen, S., Frantz, D., Hagolle, O., Hollstein, A., Kirches, G., Li, F., Louis, J., Mangin, A., Pahlevan, N., Pflug, B., and Vanhellemont, Q. (2018). Atmospheric correction inter-comparison exercise. *Remote Sensing*, 10(3):352. 886
887
888
889
- Duveiller, G., Baret, F., and Defourny, P. (2011). Crop specific green area index retrieval from MODIS data at regional scale by controlling pixel-target adequacy. *Remote Sensing of Environment*, 115(10):2686–2701. 890
891
892
893
- Eskes, H. J., Antonakaki, T., Basart, S., Benedictow, A., Blechschmidt, A.-M., Chabrillat, S., Christophe, Y., Clark, H., Cuevas, E., Hansen, K. M., and Others (2018). Upgrade verification note for the CAMS near-real time global atmospheric composition service: Evaluation of the e-suite (experiment gkvv) for the period April 2016-October 2016. Technical report, Copernicus. 894
895
896
897
898
899
- Fraser, R. and Kaufman, Y. (1985). The relative importance of aerosol scattering and absorption in remote sensing. *IEEE Transactions on Geoscience and Remote Sensing*, GE-23(5):625–633. 900
901
902
- Gómez-Dans, J. L., Lewis, P. E., and Disney, M. (2016). Efficient emulation of radiative transfer codes using gaussian processes and application to land surface parameter inferences. *Remote Sensing*, 8(2):119. 903
904
905
906

- Gorroño, J., Fomferra, N., Peters, M., Gascon, F., and others (2017). A radiometric uncertainty tool for the Sentinel 2 mission. *Remote Sensing*. 907
908
909
- Gorroño, J., Hunt, S., Scanlon, T., Banks, A., Fox, N., Woolliams, E., Underwood, C., Gascon, F., Peters, M., Fomferra, N., Govaerts, Y., Lamquin, N., and Bruniquel, V. (2018). Providing uncertainty estimates of the Sentinel-2 top-of-atmosphere measurements for radiometric validation activities. *European Journal of Remote Sensing*, 51(1):650–666. 910
911
912
913
914
915
- Guanter, L., Del Carmen González-Sanpedro, M., and Moreno, J. (2007). A method for the atmospheric correction of ENVISAT/MERIS data over land targets. *International journal of remote sensing*, 28(3-4):709–728. 916
917
918
919
- Guanter, L., Richter, R., and Kaufmann, H. (2009). On the application of the MODTRAN4 atmospheric radiative transfer code to optical remote sensing. *International Journal of Remote Sensing*, 30(6):1407–1424. 920
921
922
923
- Hagolle, O., Huc, M., Pascual, D., and Dedieu, G. (2015). A multi-temporal and multi-spectral method to estimate aerosol optical thickness over land, for the atmospheric correction of FormoSat-2, LandSat, VENS and sentinel-2 images. *Remote Sensing*, 7(3):2668–2691. 924
925
926
927
928
- Hsu, N., Tsay, S.-C., King, M., and Herman, J. (2004). Aerosol properties over bright-reflecting source regions. *IEEE Transactions on Geoscience and Remote Sensing*, 42(3):557–569. 929
930
931
- Hsu, N. C., Jeong, M.-J., Bettenhausen, C., Sayer, A. M., Hansell, R., Seftor, C. S., Huang, J., and Tsay, S.-C. (2013). Enhanced deep blue aerosol retrieval algorithm: The second generation. *Journal of Geophysical Research: Atmospheres*, 118(16):9296–9315. 932
933
934
935
- Ju, J., Roy, D. P., Vermote, E., Masek, J., and Kovalskyy, V. (2012). Continental-scale validation of MODIS-based and LEDAPS landsat ETM+ atmospheric correction methods. *Remote Sensing of Environment*, 122:175–184. 936
937
938
939
- Kaiser, G. and Schneider, W. (2008). Estimation of sensor point spread function by spatial subpixel analysis. *International Journal of Remote Sensing*, 29(7):2137–2155. 940
941
942
- Kaminski, T., Pinty, B., Voßbeck, M., Lopatka, M., Gobron, N., and Robustelli, M. (2017). Consistent retrieval of land surface 943
944

- radiation products from EO, including traceable uncertainty estimates. *Biogeosciences*, 14(9):2527–2541. 945
946
- Kaufman, Y. J., Tanré, D., Remer, L. A., Vermote, E. F., Chu, A., and Holben, B. N. (1997). Operational remote sensing of tropospheric aerosol over land from EOS moderate resolution imaging spectroradiometer. *Journal of Geophysical Research: Atmospheres*, 102(D14):17051–17067. 947
948
949
950
951
- Levy, R. C., Remer, L. A., and Dubovik, O. (2007a). Global aerosol optical properties and application to moderate resolution imaging spectroradiometer aerosol retrieval over land. *Journal of Geophysical Research: Atmospheres*, 112(D13):n/a–n/a. 952
953
954
955
- Levy, R. C., Remer, L. A., Mattoo, S., Vermote, E. F., and Kaufman, Y. J. (2007b). Second-generation operational algorithm: Retrieval of aerosol properties over land from inversion of moderate resolution imaging spectroradiometer spectral reflectance. *Journal of Geophysical Research: Atmospheres*, 112(D13):n/a–n/a. 956
957
958
959
960
- Lewis, P., Gómez-Dans, J., Kaminski, T., Settle, J., Quaife, T., Gobron, N., Styles, J., and Berger, M. (2012). An earth observation land data assimilation system (eo-ldas). *Remote Sensing of Environment*, 120:219–235. 961
962
963
964
- Li, X. and Strahler, A. (1992). Geometric-optical bidirectional reflectance modeling of the discrete crown vegetation canopy: effect of crown shape and mutual shadowing. *IEEE Transactions on Geoscience and Remote Sensing*, 30(2):276–292. 965
966
967
968
- Liang, S. (2001). Narrowband to broadband conversions of land surface albedo I: Algorithms. *Remote sensing of environment*, 76(2):213–238. 969
970
- Liang, S., Zhong, B., and Fang, H. (2006). Improved estimation of aerosol optical depth from MODIS imagery over land surfaces. *Remote Sensing of Environment*, 104(4):416–425. 971
972
973
- Lucht, W. and Lewis, P. (2000). Theoretical noise sensitivity of BRDF and albedo retrieval from the EOS-MODIS and MISR sensors with respect to angular sampling. *International Journal of Remote Sensing*, 21(1):81–98. 974
975
976
977
- Luffarelli, M., Govaerts, Y., Goossens, C., Wolters, E. L. A., and Swinnen, E. (2017). Joint retrieval of surface reflectance and aerosol properties from PROBA-V observations, part I: Algorithm performance evaluation. In *2017 9th International Workshop on the* 978
979
980
981

<i>Analysis of Multitemporal Remote Sensing Images (MultiTemp)</i> , pages 1–6.	982 983
Lyapustin, A., Martonchik, J., Wang, Y., Laszlo, I., and Korkin, S. (2011a). Multiangle implementation of atmospheric correction (MAIAC): 1. radiative transfer basis and look-up tables. <i>Journal of Geophysical Research</i> , 116(D3).	984 985 986 987
Lyapustin, A., Wang, Y., Laszlo, I., Kahn, R., Korkin, S., Remer, L., Levy, R., and Reid, J. (2011b). Multiangle implementation of atmospheric correction (maiac): 2. aerosol algorithm. <i>Journal of Geophysical Research: Atmospheres</i> , 116(D3).	988 989 990 991
Lyapustin, A. I. and Kaufman, Y. J. (2001). Role of adjacency effect in the remote sensing of aerosol. <i>Journal of geophysical research</i> , 106(D11):11909–11916.	992 993 994
Lyapustin, A. I., Wang, Y., Laszlo, I., Hilker, T., Hall, F. G., Sellers, P. J., Tucker, C. J., and Korkin, S. V. (2012). Multi-angle implementation of atmospheric correction for modis (maiac): 3. atmospheric correction. <i>Remote Sensing of Environment</i> , 127:385–393.	995 996 997 998
Masek, J., Vermote, E., Saleous, N., Wolfe, R., Hall, F., Huemmrich, F., Gao, F., Kutler, J., and Lim, T. (2012). Ledaps landsat calibration, reflectance, atmospheric correction preprocessing code.	999 1000 1001
Mira, M., Weiss, M., Baret, F., Courault, D., Hagolle, O., Gallego-Elvira, B., and Oliso, A. (2015). The modis (collection v006) brdf/albedo product mcd43d: Temporal course evaluated over agricultural landscape. <i>Remote Sensing of Environment</i> , 170:216–228.	1002 1003 1004 1005
Muller, J.-P., Lewis, P., Bréon, F.-M., Bacour, C., Price, I., Chaumat, L., Prunet, P., Gonzales, L., Schlundt, C., Vountas, M., et al. (2013). A surface reflectance database for esa’s earth observation missions (adam).	1006 1007 1008 1009
Ouaidrari, H. and Vermote, E. F. (1999). Operational Atmospheric Correction of Landsat TM Data. <i>Remote sensing of environment</i> , 70(1):4–15.	1010 1011 1012
Pahlevan, N., Sarkar, S., Franz, B., Balasubramanian, S., and He, J. (2017). Sentinel-2 MultiSpectral instrument (MSI) data processing for aquatic science applications: Demonstrations and validations. <i>Remote Sensing of Environment</i> , 201:47–56.	1013 1014 1015 1016
Pearson, N. C., Livo, K. E., Driscoll, R. L., Lowers, H. A., Hoefen, T. M., Swayze, G. A., Klein, A. J., Kokaly, R. F., Wise, R. A., Benzel, W. M., and Clark, R. N. (2017). Usgs spectral library version 7 data.	1017 1018 1019

- Pérez-Ramírez, D., Whiteman, D. N., Smirnov, A., Lyamani, H., Holben, B. N., Pinker, R., Andrade, M., and Alados-Arboledas, L. (2014). Evaluation of AERONET precipitable water vapor versus microwave radiometry, GPS, and radiosondes at ARM sites. *Journal of Geophysical Research: Atmospheres*, 119(15):9596–9613.
- Pfeifer, M., Disney, M., Quaife, T., and Marchant, R. (2012). Terrestrial ecosystems from space: a review of earth observation products for macroecology applications. *Global ecology and biogeography: a journal of macroecology*, 21(6):603–624.
- Quaife, T. and Lewis, P. (2010). Temporal constraints on linear BRDF model parameters. *IEEE Transactions on Geoscience and Remote Sensing*, 48(5):2445–2450.
- Remer, L. A., Kaufman, Y. J., Tanré, D., Mattoo, S., Chu, D. A., Martins, J. V., Li, R.-R., Ichoku, C., Levy, R. C., Kleidman, R. G., Eck, T. F., Vermote, E., and Holben, B. N. (2005). The MODIS aerosol algorithm, products, and validation. *Journal of the Atmospheric Sciences*, 62(4):947–973.
- Ross, J. (1981). *The radiation regime and architecture of plant stands (Tasks for Vegetation Science)*. Springer.
- Roujean, J.-L., Leroy, M., and Deschamps, P.-Y. (1992). A bidirectional reflectance model of the Earth's surface for the correction of remote sensing data. *Journal of Geophysical Research, D: Atmospheres*, 97(D18):20455–20468.
- Rouquié, B., Hagolle, O., Bréon, F.-M., Boucher, O., Desjardins, C., and Rémy, S. (2017). Using Copernicus Atmosphere Monitoring Service Products to Constrain the Aerosol Type in the Atmospheric Correction Processor MAJA. *Remote Sensing*, 9(12):1230.
- Roy, D., Zhang, H., Ju, J., Gomez-Dans, J., Lewis, P., Schaaf, C., Sun, Q., Li, J., Huang, H., and Kovalskyy, V. (2016). A general method to normalize landsat reflectance data to nadir brdf adjusted reflectance. *Remote Sensing of Environment*, 176:255–271.
- Schaaf, C. B., Gao, F., Strahler, A. H., Lucht, W., Li, X., Tsang, T., Strugnell, N. C., Zhang, X., Jin, Y., Muller, J.-P., et al. (2002). First operational brdf, albedo nadir reflectance products from modis. *Remote sensing of Environment*, 83(1):135–148.
- Schläpfer, D., Borel, C. C., Keller, J., and Itten, K. I. (1998). Atmospheric Precorrected Differential Absorption Technique to

-
- Retrieve Columnar Water Vapor. *Remote sensing of environment*, 65(3):353–366. 1057
1058
- Schowengerdt, R. A. (2006). *Remote Sensing: Models and Methods for Image Processing*. Academic Press. 1059
1060
- Shepherd, J. D. and Dymond, J. R. (2003). Correcting satellite imagery for the variance of reflectance and illumination with topography. *International journal of remote sensing*, 24(17):3503–3514. 1061
1062
1063
- Tan, B., Woodcock, C., Hu, J., Zhang, P., Ozdogan, M., Huang, D., Yang, W., Knyazikhin, Y., and Myneni, R. (2006). The impact of gridding artifacts on the local spatial properties of modis data: Implications for validation, compositing, and band-to-band registration across resolutions. *Remote Sensing of Environment*, 105(2):98–114. 1064
1065
1066
1067
1068
- Vermote, E., Tanre, D., Deuze, J., Herman, M., and Morcette, J.-J. (1997). Second simulation of the satellite signal in the solar spectrum, 6s: an overview. *IEEE Transactions on Geoscience and Remote Sensing*, 35(3):675–686. 1069
1070
1071
1072
- Wang, Z., Schaaf, C. B., Sun, Q., Shuai, Y., and Román, M. O. (2018). Capturing rapid land surface dynamics with Collection V006 MODIS BRDF/NBAR/Albedo (MCD43) products. *Remote sensing of environment*, 207:50–64. 1073
1074
1075
1076
- Wanner, W., Strahler, A. H., Hu, B., Lewis, P., Muller, J.-P., Li, X., Schaaf, C. L. B., and Barnsley, M. J. (1997). Global retrieval of bidirectional reflectance and albedo over land from EOS MODIS and MISR data: Theory and algorithm. *Journal of Geophysical Research: Atmospheres*, 102(D14):17143–17161. 1077
1078
1079
1080
1081
- Wulder, M. A., Hilker, T., White, J. C., Coops, N. C., Masek, J. G., Pflugmacher, D., and Crevier, Y. (2015). Virtual constellations for global terrestrial monitoring. *Remote Sensing of Environment*, 170:62–76. 1082
1083
1084
1085
- Zhu, C., Byrd, R. H., Lu, P., and Nocedal, J. (1997). Algorithm 778: L-BFGS-b: Fortran subroutines for large-scale bound-constrained optimization. *ACM Transactions on Mathematical Software*, 23(4):550–560. 1086
1087
1088
1089